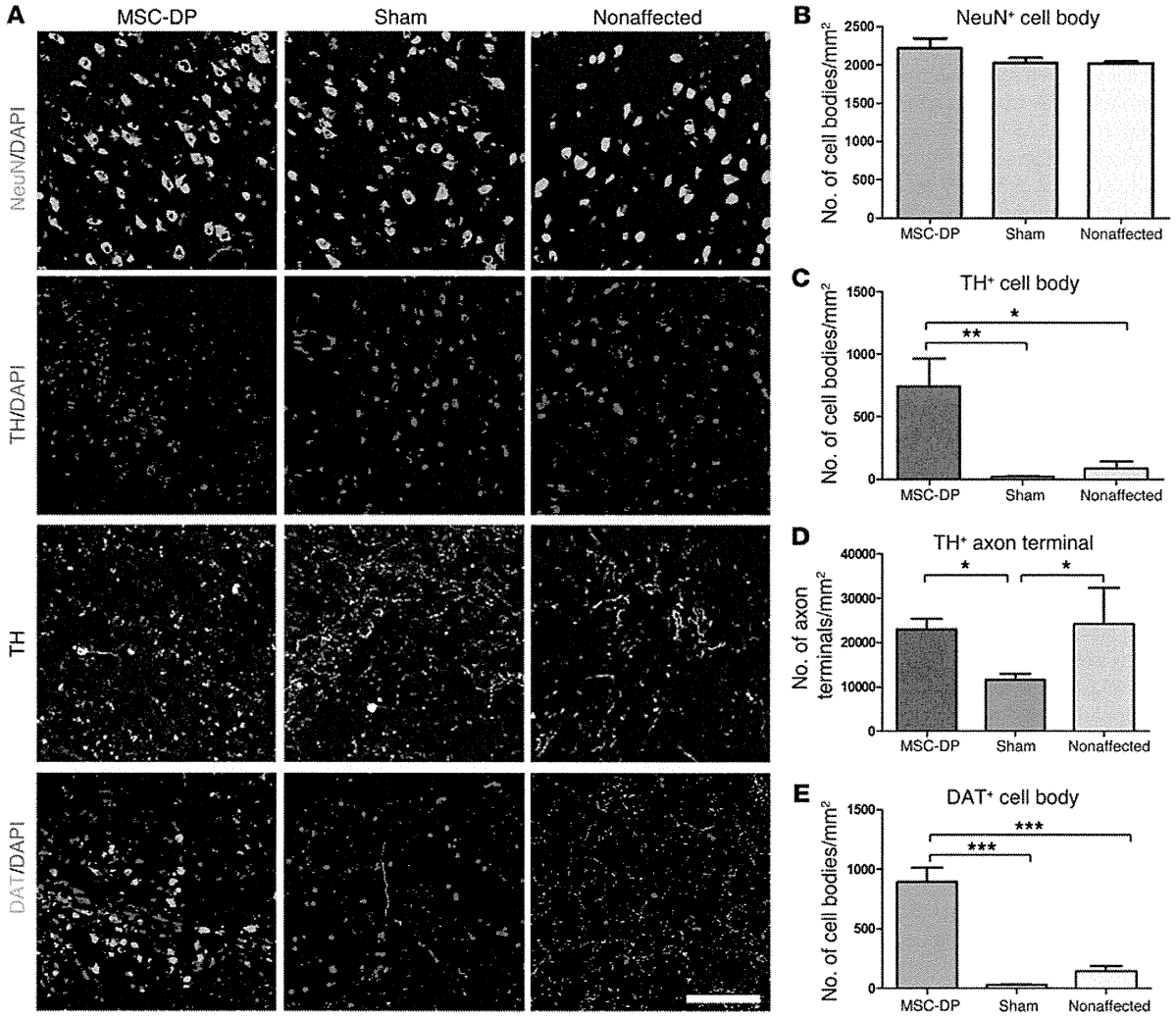

Figure 6

Quantitative analysis of immunohistochemistry of the dorsal posterior striatum. (**A**) Immunohistochemical sections of the dorsal posterior striatum for NeuN, TH$^+$ cells, TH$^+$ terminals, and DAT$^+$ cells in MSC-DP cell–engrafted animals (MSC-DP), in the sham-operated striatum (Sham), and in the non-MPTP–treated side of the striatum (nonaffected) of sham animals. Scale bar: 100 μm. (**B**) Cell counts of NeuN$^+$ and (**C**) TH$^+$ neuronal cell bodies, (**D**) TH$^+$ axon terminals, and (**E**) DAT$^+$ neurons in the dorsal posterior striatum were plotted for each group. *$P < 0.05$, **$P < 0.01$, ***$P < 0.001$, Bonferroni-corrected multiple comparisons.

applying stem cells are functionality and safety issues after graft, both of which need to be overcome before clinical trials can be commenced (40). From these standpoints, we examined whether the MSC-DP cells could safely function in primate PD model.

Our results can be summarized into the four points. First, the MSC-DP cells induced from macaque MSCs were confirmed to express markers for Tuj1, MAP-2, TH, and DAT and to release dopamine in vitro, as shown previously (21). Moreover, they expressed GIRK2 and FOXA2, specific markers of A9 dopaminergic neurons, but not calbindin, a marker of A10 neurons. Second, when MSC-DP cells were autologously engrafted into the striatum of hemiparkinsonian macaques, motor behaviors, as assessed by CRS and the hand-reach task, gradually improved without accompanying dyskinesia. PET scans detected distinct binding of ^{11}C-CFT in the engrafted striatum initially, followed by an exponential decrease in ^{11}C-CFT binding. Kinetic analysis suggested that a portion of the MSC-DP graft showed levels of ^{11}C-CFT binding above the baseline over a period of 7 months. Third, immunohistochemical analysis at 9 months confirmed the increase of DAT$^+$/TH$^+$/GIRK2$^+$ cells and the TH$^+$ axon terminals in the engrafted striatum. Fourth, no tumorigenicity was suspected by peripheral blood tests, blood tumor markers, ^{18}F-FDG PET scans, and histology. Therefore, MSC-DP cells are likely to be nontumorigenic and able to remain in the transplanted region until at least 9 months after engraftment, although not in large quantities, thereby modestly restoring dopaminergic function and motor behaviors in vivo.

To the best of our knowledge, this study is the first to show restoration of dopaminergic function and motor behaviors in parkinsonian primate animals following engraftment of MSC-de-

rived cells. It is notable that kinetic analysis of ^{11}C-CFT binding and histology results suggested that at least a portion of MSC-DP cells survived in situ for over 9 months. This is in contrast to naive MSCs, which have much shorter survival times in the brain and disappeared within 3 months in rodent studies; one possible reason for this could be senescent or apoptotic changes (12, 13). The long-term survival of MSC-DP cells may have been accompanied by gradual integration into or reinnervation of the host striatal tissues. As shown in Figure 6D, increased numbers of TH$^+$ terminals were observed in engrafted animals compared with control animals, suggesting formation of new synaptic connections between the engrafted cells and host tissues; this may at least in part underlie the motor recovery observed at a later time after transplantation of MSC-DP cells. The fact that in vitro DArc was correlated with ^{11}C-CFT binding only at early time points after engraftment also supports the hypothesis that other mechanisms, such as integration of MSC-DP cells, into host tissues may be critical for full restoration of motor function.

A notable feature of the current MSC-DP cells is their similarity to A9 dopaminergic neurons. Previously, we reported that dopaminergic neuron-like cells are inducible from MSCs by genetic introduction of *NICD*, followed by cytokine treatment with bFGF, forskolin, CNTF, and GDNF (20, 21). This report further characterized the MSC-DP cells and found that they were double positive for FOXA2 and GIRK2, both specific markers of differentiated A9 dopaminergic neurons. In particular, FOXA2 was recently identified as a transcription factor required for specifying and maintaining the dopaminergic neuron phenotype (28, 42) and is considered to be expressed exclusively in floor plate–derived dopaminergic neurons (43). We confirmed the coexpression of FOXA2 and GIRK2 in SNc tissue that contains A9 dopaminergic neurons but not in the VTA, which contains A10 dopaminergic neurons. GIRK2/FOXA2 double-positive cells have not been induced from other stem cell sources using existing protocols (44–46), except for one that manipulates both the sonic hedgehog and WNT signaling pathways (43, 47). Recent studies of fetal tissue engrafting in patients with PD or PD model rats have shown that A9 dopaminergic neurons are determinants of successful functional recovery (16, 48) and decreased dyskinesia (49) and that they are associated with well-organized synaptic connectivity (16). Overall, the results of our study support a recent hypothesis that well-differentiated stem cells offer benefits for both survival and functional integration with host neural tissues (47).

There are 2 points that favor the suitability of MSC-DP cell transplantation for clinical application. First, the current strategy rests on the autologous cell system. This offers advantages over allograft systems, such as fetal tissue engrafting, in terms of the ethical, social, and political implications. MSCs can be easily collected autologously from the patients' own bone marrow aspirates. Aspiration of bone marrow by itself is widely applied in the field of hematology, and infusion of bone marrow from HLA-matched donors is also commonly performed for treatment of leukemia. Moreover, bone marrow–derived MSC transplantation into brain has been tried clinically without any safety problems (10). The autologous system also has the advantage of not requiring immunosuppression, as compared with allograft systems. Second, no tumorigenicity was suspected up to 9 months after engraftment in primates. Adult stem cells, including MSCs, are known to have less tumorigenic proliferative activity than other cell sources, such as embryonic stem cells. Moreover, the MSC-DP cells expressed MAP-2, a marker of postmitotic neurons (50), suggesting that they possess minimal risk of tumor formation. A previous study in which MSC-DP cells were engrafted into rodents consistently showed no evidence of tumorigenicity during a 14-week period (20). Schwann cells derived from MSCs also showed no tumorigenicity during a 1-year observation period in our previous study in primates (18). The differentiation technique for converting naive MSCs to MSC-DP cells involved *NICD* gene introduction by transfection of a plasmid gene but not by retrovirus- or lentivirus-mediated gene transfer, which is known to modify the nuclear genome. The introduced plasmid *NICD* gene does not appear to have a prolonged effect on the cell cycle, because the introduced *NICD* gene did not remain in MSCs for a long time (for no longer than 2 passages) (51).

Although our study showed a potential therapeutic effect of MSC-DP cells in a PD model, one may argue that cells pushed to full maturity in vitro would not be the best cell source for grafting (2). For example, grafted dopaminergic neurons obtained from fetal brain are known to survive poorly if their maturation has passed a narrow optimal time window at the time of harvesting (52). Such an argument might be applicable to our results in that the rapid loss of ^{11}C-CFT binding over time may have been a consequence of the use of differentiated MSCs, namely MSC-DP cells. However, this is still an open question, particularly with respect to stem cells; the relationship between in vitro maturity and survival after graft is not simple and may also depend on other factors, such as the types of cell sources and in vitro preparation. ES grafts with very immature cells seem to cause tumorigenicity, while relatively immature cells, such as neural precursors/neuroblasts, suffer from poor cell survival (40). But more highly differentiated DA neurons recently engineered from ES cells showed good survival (47). Undifferentiated MSCs are known to die very rapidly, within several days after being engrafted into the brain, and this seems to be due to facilitated senescence (12) or programmed cell death of the MSCs (13). Therefore, we have followed the working hypothesis, testing well-differentiated cells derived from MSCs. To address the issue of optimal maturity, cell marker–based subtyping should also be standardized in future studies (33).

A few issues suggest the need for some caution when interpreting our results. First, in this study, we did not label the MSC-DP cells by tagging them with, for example, green fluorescent protein in order to trace the cells after transplantation. This was because we avoided using any extrinsic factors that may pose a safety concern or affect cell survival. As a result, the dopaminergic neuron-like cells found in the striatum may not truly have originated from the grafted MSC-DP cells. However, this is unlikely because the striatum in primates has only a few dopaminergic neurons under normal circumstances: TH$^+$ cells number <1% of striatal neurons (53) and are preferentially scattered near the white matter–ventral striatum border. In our case, the TH$^+$/DAT$^+$/GIRK2$^+$ cells were located only in an area near the engrafted area in the dorsal striatum (Figure 5), and the number of the cells was larger than that in sham and nonaffected striata (Figure 6, C and E). Second, regarding PET ligands, a well-known ligand for DA, ^{18}F-DOPA was not used in this study, because it is a metabolic ligand for amino acids and may reflect not only dopamine turnover in dopaminergic neurons, but also uptake of amino acid precursors in tumors (54) or inflammation (55). Therefore, ^{11}C-CFT was carefully chosen as an in vivo surrogate marker for tracking MSC-DP cells, because it is a highly specific ligand for DAT, which is specif-

ically expressed in dopaminergic neurons and was confirmed to be present in the current MSC-DP cells in vitro. The high uptake of ^{11}C-CFT was not found in any of the sham-operated animals, even though they received PBS injections, which may induce tissue damage or inflammation. Third, the study does not clarify the complete mechanism underlying the motor recovery in the current animals. PET findings revealed increased DAT expression only in the early phase, while behavioral data showed significant recovery only in the later phase. As described above, we believe the discrepancy is explained by a time delay required for the remaining MCS-DP cells to achieve synaptic connections with the host tissues. This speculation should be clarified in the future study, since the delayed motor recovery found here seems to be common in trials of cell replacement therapies in PD. For example, fetal tissue grafting improved motor symptoms at 6 to 9 months after grafting in selected patients with PD (39). ES cell–derived well-differentiated DA neurons also restored motor behaviors 3–5 months after grafting in an animal model (47). Finally, these data do not show convincing evidence that benefits were truly results of an in vitro process differentiating MSCs into A9 DA neurons. We cannot completely exclude the possibility that undifferentiated MSCs, contaminated in the graft and not positive for A9 markers (25%–50% of cells; Figure 1K), might have contributed to the observed benefits, for example, by way of trophic effects. Therefore, future studies should directly compare the MSC-DP cell with naive MSC transplantation.

In conclusion, this study indicates that the autologous MSC-differentiation system may be safe and potentially effective for restoring motor dysfunction in hemiparkinsonian nonhuman primate animals. Although further studies are needed to improve the viability of MSC-DP cells and net performance for functional recovery, the current system may expand the availability of cell sources for cell-based therapies for patients with PD.

Methods

Ten adult male cynomolgus monkeys (*Macaca fascicularis*; body weight, 3–4 kg) were used in this study. All animals were housed in a room kept at 26°C. Animals were pretreated with the neurotoxin MPTP to generate a hemiparkinsonian model, and their bone marrow aspirates were used for induction of autologous MSC-DP cells. Five animals were used for the engraftment of MSC-PD cells (n = 5, MSC-DP group), and the remaining 5 underwent a sham operation in which they received injection of PBS only (n = 5, sham group).

Isolation of MSCs from bone marrow aspirates. Primary MSCs were isolated from bone marrow aspirates obtained from the iliac bone of every animal in the engrafted group. Bone marrow was aspirated from each animal 3–4 months prior to transplantation under deep anesthesia achieved by intramuscular injection of ketamine (6.6 mg/kg), xylazine (1.3 mg/kg), and atropine (0.01 mg/kg). For aspiration, we used a bone marrow needle (18 G; Sheen-man Co. Ltd.) and 2.5-ml aspiration syringes containing 100 units of heparin (Novo-Heparin, Mochida Pharmaceutical Co. Ltd.) to prevent clotting. Aspirates were diluted 1:10 using culture medium (α-minimum essential medium [α-MEM] plus 15% FBS plus 2 mM L-glutamine plus kanamycin) and incubated at 37°C in 5% CO_2. After 4 days, nonadherent cells were removed by replacing the medium. Adherent cells, namely, MSCs, were subjected to subculture when they reached 95% confluence and were subcultured 4 times. Finally, they were subjected to dopaminergic neuronal differentiation.

Differentiation of MSC-DP cells from MSCs. MSC-DP cells were differentiated from MSCs using a method of spermine-pullulan–mediated reverse transfection, as described previously (21). We used pullulan, with an average molecular weight of 47,300 Da (Hayashibara Biochemical Laboratories) and spermine (Sigma-Aldrich). A cationized pullulan derivative was prepared as described previously (21), and a gene encoding mouse NICD (constitutively active form), including a transmembrane region with a small fragment of extracellular domain and the entire intracellular domain, was subcloned into the pCI-neo vector (Promega) (pCI-NICD). Cells were further selected by G418 for 3 to 4 days, replated at a cell density of 2,080 cells per cm^2, and treated with 5 μM forskolin (Calbiochem), 10 ng/ml bFGF (Peprotech), and 10 ng/ml CNTF (R&D Systems) in α-MEM containing 5% FBS for 5 days. Finally, GDNF (50 ng/ml; Peprotech) was added.

Evaluation of MSC-DP cells — dopamine release assay using HPLC. The dopamine release assay was performed as described previously (20, 21). Briefly, cells were washed in a low K^+ solution for 5 minutes, and the medium was replaced with a high K^+ solution for 5 minutes. The concentration of released dopamine was determined using HPLC with a reverse-phase column and an electrochemical detector system (Eicom Corporation). The mobile phase was composed of 0.1 M phosphate buffer (pH 6.0), 20% methanol. The amount of dopamine release was measured according to the number of cells, which were counted after trypsinization.

Evaluation of MSC-DP cells — immunocytochemistry. The primary antibodies used were anti-MAP-2ab (1:250; Sigma-Aldrich) and anti-Tuj1 (1:100; BAbCO) as neuron-specific markers and anti-TH (1:1,000; Chemicon, Millipore), anti-DAT (1:100; Millipore), anti-GIRK2 (1:80; Alomone Labs), and anti-FOXA2 (1:50; Santa Cruz Biotechnology Inc.) as markers of dopaminergic neurons. We also used an anti–sodium channel antibody (PAN) (clone K58/35, 1:1,000; Sigma-Aldrich) as a marker of neurons. Secondary antibodies were anti-mouse or anti-rabbit IgG antibodies conjugated to Alexa Fluor 488 (Invitrogen) and anti-rabbit or anti-goat IgG conjugated to Cy3 (Jackson ImmunoResearch Laboratory). Nuclei were counterstained with DAPI and inspected using confocal laser microscopy (Nikon Corporation).

Evaluation of MSC-DP cells — RT-PCR. We analyzed the relative expression levels of *GIRK2*, *FOXA2*, and *CALB1* mRNAs using RT-PCR to classify MSC-DP cells as A9-type neurons (*GIRK2*$^+$/*FOXA2*$^+$/*CALB1*$^-$) or A10-type neurons (*GIRK2*$^-$/*FOXA2*$^-$/*CALB1*$^+$) (28, 29, 56). The amount of cDNA was normalized on the basis of the signal from the ubiquitously expressed β-actin. The primers were designed based on the cDNA sequence of the *Macaca mulatta*, which is highly homologous to that of *Rattus norvegicus*, as revealed by an alignment search tool (BLAST; http://www.ncbi.nlm.nih.gov/BLAST/). The primer sequences and precise conditions were as follows: β-actin, 5′-TCTAGGCGGACTGTGACTTACTTGCGTTAC-3′ (forward) and 5′-AATCAAAGTCCTCGGCCACATTGTAGAACT-3′ (reverse) (TM, melting temperature; 60°C, 25 cycles); GIRK2, 5′-ATCCAGAGGTATGTGAGGAAAGATG-3′ (forward) and 5′-CACTGTGTAAACCATGACGAAAATC-3′ (reverse) (TM, melting temperature; 55°C, 40 cycles); calbindin, 5′-GCTGTATGATCAGGACGGCAAT-3′ (forward) and 5′-TCTAGTTATCCCCAGCACAGAGAA-3′ (reverse) (TM, melting temperature; 58°C, 40 cycles); and FOXA2, 5′-CGGTGTTGCAGAGACGAAAG-3′ (forward) and 5′-CAGAATCTGCAGGTGCTTGAAG-3′ (reverse) (TM, melting temperature; 58°C, 40 cycles). As a positive control for GIRK2, FOXA2, and calbindin, total RNA was collected and analyzed using 2 types of brain tissues from cynomolgus embryos (~6th fetal month, *Macaca fascicularis*) and an adult animal (8 years old, *Macaca fascicularis*), namely, the SNc and VTA.

MPTP-induced hemiparkinsonism. The animal model of the unilateral PD was produced using the neurotoxin MPTP, as previously reported (30, 57), with some modifications. Briefly, animals received slow arterial injections of MPTP into the right carotid artery. Unlike previous studies that accessed the carotid artery by incision of the upper cervical area, we

applied an angiographic approach that allowed us to access the target artery less invasively and did not require postoperative occlusion of the target artery, which causes insufficient cerebral circulation. We used an 80-cm-long catheter (3F, CATEX Co. Ltd.) and X-ray angiographic device (OEC 8800, GE Healthcare) to place the catheter into the internal carotid artery. After the tip of the catheter was placed in the proximal (cervical) portion of the internal carotid artery, the MPTP solution (0.4 mg/kg dissolved in 40 ml of saline, pH 7.4) was infused at a rate of 2 ml per minutes. In every animal, the right pupil showed dilatation with a diameter >5 mm, indicating the adrenergic effect of MPTP (58). All animals recovered safely from anesthesia and exhibited hemiparkinsonism with a crooked arm posture and dragging leg, with slow or disabled movements in the left hand and arm. All animals continuously revealed hemiparkinsonism over a period of 3 months, and none of them showed spontaneous recovery from motor disabilities.

Engrafting MSC-DP cells into the striatum. Under deep anesthesia, each animal in the engraftment group underwent MRI-guided stereotactic surgery for engrafting of MSC-DP cells into the putamen on the right side (the same side as the MPTP infusion). The animal's head was fixed to a stereotactic acrylic holder in a sphinx position, the head skin and muscles were incised under aseptic conditions after subcutaneous injection of lidocaine (Xylocain 2%, AstraZeneca PLC), and the surface of the cranium bone was exposed by separating the galea aponeurotica. Three to four MRI-visible markers were attached to the fringe of the exposed cranium to be used as a reference for co-registering the translocation between MRI and the stereotactic micromanipulator. Then, the stereotactic holder was placed horizontally on the MRI gantry with its axis parallel to the *z* axis of the MRI bore, and a high-resolution head MRI scan was obtained with the inversion recovery-fast spoiled gradient recalled echo (IR-FSPGR) sequence. Obtained MRI images were transformed with a 3D translocation algorithm to the standard macaque brain template (31) and resliced in a volume with a matrix of 110,134,80 voxels, a cubic voxel size of 0.5-mm edge length, and an origin at the midportion of the anterior commissure (AC). On 3 coronal views of the MRI image sectioned at AC −5, −7, and −9 mm, we determined 12 target points for transplantation (Figure 3A). For each of the 12 targets, the relative coordinates were read on the MRI image in reference to one of the markers on the cranium. After MRI scans were finished, the head holder was then attached to a customized metallic stereotaxic apparatus on which the stereotactic coordinates of the markers were read using a micromanipulator (SM-15 Narishige Group). Then the target coordinates in the micromanipulator were determined based on the coordinates of the reference markers in the MRI image and their location relative to that of the micromanipulator.

Immediately before injecting cells, the autologous MSC-DP cells were collected and suspended in 60 μl of 0.1 M PBS, and the number of cells was counted. The average total cell count was $14.0 \times 10^6 \pm 5.0 \times 10^6$ (mean ± SD), with a range of 9.0×10^6 to 20.4×10^6 (Table 1). For each target coordinate of *x* and *y* determined by above method, the tip of a 10-μl Hamilton syringe with a 30-gauge needle was slowly advanced vertically and kept in place at the target coordinate for *z*. Then MSC-DP cells in PBS solution were injected at a rate of 0.5 μl per minute until a total of 5 μl had been injected at each target site. The needle was kept in place for an additional 3 minutes to allow the injectate to diffuse and then slowly retracted to minimize diffusion of the injectate over the cortical surface. The sham operation group received injection of the same amount of PBS solution in the same 12 target points in the right dorsal posterior putamen.

Behavioral analysis of motor function. Behavioral performance was assessed using the CRSs, hand-reach scores for the affected hands, and spontaneous activities in housing cages. The previously validated CRSs were used to quantitatively assess the parkinsonian status of the monkeys (59, 60). The scale consists of ratings of posture (0 to 2), gait (0 to 5), bradykinesia (0 to 5), balance (0 to 2), tremor for each arm (0 to 3), gross motor skills (0 to 4 for each arm), defense reaction (0 to 2), and freezing (0 to 2). The score was the sum of the features out of a total of 32 points, with 0 corresponding to normal and 32 corresponding to severe disability. Scores were assessed before and 14 days, 2 months, 4 months, and 8 months after engrafting and were evaluated by an experimenter blinded to the group allocation.

Hand-reach scores were assessed based on food-taking behavior by the affected hand, as described previously (30, 61), and were assessed at the same time points as CRSs (before and 14 days, 2 months, 4 months, and 8 months after engraftment). Five ~5-mm^3 pieces of apple were placed in front of a circular hole (6-cm diameter) in the lower corner of the cage, so that the animals could pick up the pieces and eat them. Five trials were performed for each session, and three sessions were performed on each of three consecutive days at each time point. Evaluations were made before engrafting and 14 days, 2 months, 4 months, and 8 months after engrafting. All behaviors during the task were monitored and recorded by video. After collection of all data, an experimenter blinded to the group allocation of animals scored the movement velocity of the proximal forelimb (arm and forearm) on a scale of 0 to 5 (0 means very fast, 5 means very slow), the movement velocity of hand grasping and finger pinching on a scale of 0 to 4, and the accuracy of food picking on a scale of 0 to 2. The sum of these items was recorded as the hand-reach score, with 11 corresponding to normal and 0 corresponding to severe disability.

We also measured spontaneous body activities by monitoring movements using a passive infrared system for monitoring spontaneous animal activities (Supermex, Muromachi Kikai Co. Ltd.) before and 14 days, 4 months and 8 months after engraftment. The animals were placed in a 600-mm-wide × 700-mm-deep × 740-mm-high cage, in which they were housed for acclimation beforehand. Activities were monitored consecutively for a period of 3 days (72 hours). The infrared sensor was attached so as to cover the whole cage in a single field of view. Data were imported to a computer and analyzed using a dedicated program for counting the number of pixels showing signal changes in a 10-minute time frame.

PET. We performed ^{11}C-CFT PET scanning to evaluate DAT expression in cynomolgus brains, as described previously (26, 62). The tracer ^{11}C-CFT was prepared by a conventional method using ^{11}C-methyl-triflate (63) and a precursor, nor[methyl-^{11}C]2-β-carbomethoxy-3-β-(4-fluorophenyl)tropane. The animals received intramuscular injections of ketamine and xyladine, followed by continuous intravenous infusion of propofol (6 mg/kg/h) to achieve anesthesia, and their respiration was assisted using an anesthetic machine (Cato, Drager) with an inspired gas mixture of O_2 and N_2 (O_2/N_2 = 30%:70%). We monitored endotidal CO_2 level ($EtCO_2$) and percutaneous oxygen saturation level (SpO_2), and, if needed, adjusted the respiration rate to achieve SpO_2 >95% and $EtCO_2$ of 35 mmHg. After achieving deep anesthesia, animals were placed on the PET gantry, and their bodies were kept warm by using a temperature managing unit (Bair Hugger Model 505, Arizant Inc.). A 15-minute transmission scan was obtained using a 68Ge/68Ga rod source for attenuation correction; then, 187 MBq of [^{11}C]-CFT was slowly injected intravenously over a period of 1 minute, before which a 2D-dynamic PET scan lasting for 60 minutes was commenced, with scan data obtained by 39 time frames (18 frames of 10 s, 6 frames of 30 s, 7 frames of 120 s, and 8 frames of 300 s). PET scans were performed on a PET scanner (ECAT ACCEL, Siemens Healthcare) that provided 47 slices in an axial field of view of 162 mm with an intrinsic transaxial resolution of 6.2 mm in full width at half maximum (64). The PET emission data were corrected for attenuation using the transmission data, and images were reconstructed in a matrix of 128, 128, 47 (x, y, z) with a voxel size of 0.86, 0.86, 3.38 mm (x, y, z) using a filtered back projection algorithm with a 2-mm Gaussian filter.

DAT binding in the brain was quantified voxel by voxel as a BP_{ND} image based on a simplified reference tissue model (65). The cerebellum was considered as a reference region and was identified by manual delineation of its boundary on a T1-weighted image that was pre-realigned to the time-integrated PET image. We also generated a tracer delivery image (R1) to be used for the next step of co-registration between the PET and MRI images. Calculation of BP_{ND} and R1 was performed using an open-source program (PyBLD; http://www.mi.med.osaka-u.ac.jp/pybld/pybld.html).

Tests for tumorigenicity and general conditions of engrafted animals. To assess the safety of our engrafting procedure, we performed blood tests, including red blood cell counts, white cell counts, and blood chemical tests, in all test animals to evaluate general conditions. We also analyzed the blood for several tumor markers among those tested in the clinic (66), including CEA, TPA, SLX, NSE, and BFP.

We also performed ^{18}F-FDG PET to assess any tumorigenic changes in the grafted area using a previously described method (18). After induction of anesthesia, we injected 185 MBq of ^{18}F-FDG and scanned the head region for a period from 40 to 60 minutes after injection. ^{18}F-FDG scans were performed in a 3D mode after the transmission scan. The reconstructed ^{18}F-FDG radioactivity image (in Bq/ml) was scaled based on the injected dose of ^{18}F-FDG per body weight of animal (Bq/g) to calculate images of standardized uptake value (SUV). The region was considered to be abnormal when the SUV was greater than 2.5 (67).

MRI. MRI was performed to enable MRI-guided stereotaxic surgery and evaluation of graft size after transplantation and for the analysis of PET data, using a 3-Tesla MRI scanner (Signa LX VAH/I, GE Healthcare). We obtained 3D T1-weighted MRI images from each animal with an IR-FSPGR sequence with imaging parameters as follows: TR = 9.4 ms, TE = 2.1 ms, TI = 600 ms, matrix = 128 × 128, field of view = 99.8 mm, slice thickness = 0.7 mm, number of slices = 100.

Immunohistochemical analysis of engrafted striatum. Nine months after transplantation, animals were sacrificed by overdose of pentobarbital and perfused transcardially with 4% paraformaldehyde in 0.1 M PBS. Brain tissues were cut into 10-μm-thick frozen coronal sections at the level of the posterior striatum (from y = −7 to −9 mm) using a cryostat. Primary antibodies used for immunohistochemistry were as follows: NeuN (1:150; Millipore), TH (1:1,200; DAKO), DAT (1:1,000; Millipore), GIRK2 (1:1,000; Chemicon, Millipore), calbindin (1:50; Swant), and Ki-67 (1:400; Thermo Scientific). Secondary antibodies were anti-rabbit IgG conjugated to Alexa Fluor 488 (Invitrogen), anti-rat IgG conjugated to Alexa Fluor 488 (Invitrogen), or anti-rabbit and anti-rat IgG conjugated to Cy3 (Jackson ImmunoResearch Laboratory). For triple staining for DAT/GIRK2/calbindin, calbindin was visualized using a anti-mouse IgG antibody conjugated to Alexa Fluor 680 (Invitrogen). Costaining with DAPI was also performed to confirm nuclear staining. For quantitative analysis, we chose 3 coronal sections, approximately located at y = −5, −7, −9 mm, and randomly selected 79–124 fields of view with an area of 0.316 × 0.316 mm^2 within the dorsal posterior putamen, and counted the number of cells stained for NeuN, TH, or DAT. The counts were compared among sections of striatum that received engraftments (MSC-DP group), those of sham-operated striatum (sham group), and those from the contralateral side of the striatum (non-MPTP–treated group) of sham-operated animals (nonaffected group). For counting TH$^+$ terminal density, images captured under a ×20 objective lens were imported into ImageJ (http://rsbweb.nih.gov/ij/); thereby, color was decomposed into red, green, and blue and thresholded for red based on the automatic isodata algorithm. To estimate the number of TH$^+$ terminals, the numbers of red particles, with sizes of >4 and <2,000 pixels (corresponding to >4 μm^2 and <4 × 10^6 μm^2), were counted. The data were expressed as the number of cells or axonal terminals per area (mm^2).

Statistics. Values are expressed as mean ± SEM. For immunohistochemistry and behavioral tests, data were analyzed using ANOVA. Differences among means were further analyzed by post-hoc multiple comparisons. The threshold for statistical significance was $P < 0.05$. Statistical analysis was performed using PRISM software (GraphPad Software Inc.).

For ^{11}C-CFT PET images, BP_{ND} images were preprocessed for voxel-based statistics using a previously described method (62). Briefly, the PET images were co-registered with MRI images (obtained at the time closest to the PET scan) using a rigid body transformation and transformed to the standard brain space of cynomolgus macaque (31). The transformation matrix of MRI images to the standard space was determined by an affine transformation algorithm. Voxel-based statistics were performed using a nonparametric permutation test (68) with 1-way ANOVA with repeated measures of BP_{ND} in the engrafted group. Permutation was performed within data from each subject, respecting the repeated-measures structure of the data. We are interested in the statistical F contrast for the effect of time in which FWE-corrected P values of less than 0.05 were applied using a threshold-free cluster enhancement (69). The significant cluster thus obtained (see Figure 3C) was used as a ROI for subsequent analyses (Figure 3, D–F). We also obtained BP_{ND} values from the contralateral (nonaffected) dorsal putamen as a control for BP_{ND} values, by ROI flipping (left-right) of the above cluster. The control values for BP_{ND} were 0.56 ± 0.12 (95% confidential interval, 0.51–0.61) in the engrafted group and 0.63 ± 0.11 (95% confidential interval, 0.59–0.67) in the sham group. Image analysis was performed using FSL tools (http://www.fmrib.ox.ac.uk/fsl).

The 1-hit model of neurodegeneration with a constant risk (32) was fitted to the time course data using BP_{ND} values obtained from the ROI in the engrafted striatum or using the graft volume of naive MSCs obtained from Figure 1 in ref. 13. The actual equation for the model was $V_G = V_0 \times exp(-ln[2] \times t/T_{1/2}) + Vp$, where the V_G is the time course of graft BP_{ND} or volume; V_0 is the initial value for V_G; exp is the exponential function; t is the time after grafting; $T_{1/2}$ is a half-life period; and Vp is plateau. Nonlinear fitting was performed using PRISM software.

Study approval. The experimental protocol and design of the study were in line with the institutional guides for animal experiments and the NIH Guide for the Care and Use of Laboratory Animals (NIH Publication No. 80-23) and were approved by the institutional committee for animal care and experiments of Tohoku University, RIKEN, and the National Cerebral and Cardiovascular Center.

Acknowledgments

We thank Noboru Teramoto, Hajime Fukuda, Hiroshi Koshino, Kyoko Shioya, Keiko Tokuda, and Akihiro Kawasaki for their technical help and Tsuyoshi Tahara and Hideki Mochizuki for their helpful comments. This study was supported by the Program for Promotion of Fundamental Studies in Health Sciences of the National Institute of Biomedical Innovation (NIBIO, 05-06, 10-05).

Received for publication July 13, 2012, and accepted in revised form September 28, 2012.

Address correspondence to: Takuya Hayashi, Functional Probe Research Laboratory, Center for Molecular Imaging Science, RIKEN, 6-7-3 Minnatojima-minamimachi, Chuo-ku, Kobe, Hyogo 650-0047, Japan. Phone: 81.78.304.7121; Fax: 81.78.304.7123; E-mail: takuya.hayashi@riken.jp. Or to: Mari Dezawa, Department of Stem Cell Biology and Histology and Department of Anatomy and Anthropology, Tohoku University Graduate School of Medicine, 2-1 Seiryo-machi, Aoba-ku, Sendai, Miyagi 980-8575, Japan. Phone: 81.22.717.8025; Fax: 81.22.717.8030; E-mail: mdezawa@med.tohoku.ac.jp.

1. Gage FH. Cell therapy. *Nature*. 1998; 392(6679 suppl):18–24.
2. Brundin P, Barker RA, Parmar M. Neural grafting in Parkinson's disease Problems and possibilities. *Prog Brain Res*. 2010;184:265–294.
3. Winkler C, Kirik D, Björklund A. Cell transplantation in Parkinson's disease: how can we make it work? *Trends Neurosci*. 2005;28(2):86–92.
4. Chen X, et al. Human bone marrow stromal cell cultures conditioned by traumatic brain tissue extracts: growth factor production. *J Neurosci Res*. 2002;69(5):687–691.
5. Pittenger MF, et al. Multilineage potential of adult human mesenchymal stem cells. *Science*. 1999;284(5411):143–147.
6. Charbord P. Bone marrow mesenchymal stem cells: historical overview and concepts. *Hum Gene Ther*. 2010;21(9):1045–1056.
7. Li Y, et al. Intracerebral transplantation of bone marrow stromal cells in a 1-methyl-4-phenyl-1,2,3,6-tetrahydropyridine mouse model of Parkinson's disease. *Neurosci Lett*. 2001;316(2):67–70.
8. Park HJ, Lee PH, Bang OY, Lee G, Ahn YH. Mesenchymal stem cells therapy exerts neuroprotection in a progressive animal model of Parkinson's disease. *J Neurochem*. 2008;107(1):141–151.
9. Blandini F, et al. Transplantation of undifferentiated human mesenchymal stem cells protects against 6-hydroxydopamine neurotoxicity in the rat. *Cell Transplant*. 2010;19(2):203–217.
10. Venkataramana NK, et al. Open-labeled study of unilateral autologous bone-marrow-derived mesenchymal stem cell transplantation in Parkinson's disease. *Transl Res*. 2010;155(2):62–70.
11. Kuroda Y, Kitada M, Wakao S, Dezawa M. Bone marrow mesenchymal cells: how do they contribute to tissue repair and are they really stem cells? *Arch Immunol Ther Exp (Warsz)*. 2011;59(5):369–378.
12. Wagner W, et al. Replicative senescence of mesenchymal stem cells: a continuous and organized process. *PLoS One*. 2008;3(5):e2213.
13. Moloney TC, et al. Survival and immunogenicity of mesenchymal stem cells from the green fluorescent protein transgenic rat in the adult rat brain. *Neurorehabil Neural Repair*. 2010;24(7):645–656.
14. Thompson L, Barraud P, Andersson E, Kirik D, Björklund A. Identification of dopaminergic neurons of nigral and ventral tegmental area subtypes in grafts of fetal ventral mesencephalon based on cell morphology, protein expression, and efferent projections. *J Neurosci*. 2005;25(27):6467–6477.
15. Mendez I, et al. Cell type analysis of functional fetal dopamine cell suspension transplants in the striatum and substantia nigra of patients with Parkinson's disease. *Brain*. 2005;128(pt 7):1498–1510.
16. Grealish S, et al. The A9 dopamine neuron component in grafts of ventral mesencephalon is an important determinant for recovery of motor function in a rat model of Parkinson's disease. *Brain*. 2010; 133(pt 2):482–495.
17. Damier P, Hirsch EC, Agid Y, Graybiel AM. The substantia nigra of the human brain. II. Patterns of loss of dopamine-containing neurons in Parkinson's disease. *Brain*. 1999;122(pt 8):1437–1448.
18. Wakao S, et al. Long-term observation of auto-cell transplantation in non-human primate reveals safety and efficiency of bone marrow stromal cell-derived Schwann cells in peripheral nerve regeneration. *Exp Neurol*. 2010;223(2):537–547.
19. Hayase M, et al. Committed neural progenitor cells derived from genetically modified bone marrow stromal cells ameliorate deficits in a rat model of stroke. *J Cereb Blood Flow Metab*. 2009; 29(8):1409–1420.
20. Dezawa M, et al. Specific induction of neuronal cells from bone marrow stromal cells and application for autologous transplantation. *J Clin Invest*. 2004; 113(12):1701–1710.
21. Nagane K, Kitada M, Wakao S, Dezawa M, Tabata Y. Practical induction system for dopamine-producing cells from bone marrow stromal cells using spermine-pullulan-mediated reverse transfection method. *Tissue Eng Part A*. 2009;15(7):1655–1665.
22. Sladek JR Jr, Collier TJ, Haber SN, Roth RH, Redmond DE Jr. Survival and growth of fetal catecholamine neurons transplanted into primate brain. *Brain Res Bull*. 1986;17(6):809–818.
23. Redmond DE, et al. Fetal neuronal grafts in monkeys given methylphenyltetrahydropyridine. *Lancet*. 1986;1(8490):1125–1127.
24. Bankiewicz KS, et al. The effect of fetal mesencephalon implants on primate MPTP-induced parkinsonism. Histochemical and behavioral studies. *J Neurosurg*. 1990;72(2):231–244.
25. Kordower JH, et al. Neurodegeneration prevented by lentiviral vector delivery of GDNF in primate models of Parkinson's disease. *Science*. 2000; 290(5492):767–773.
26. Takagi Y, et al. Dopaminergic neurons generated from monkey embryonic stem cells function in a Parkinson primate model. *J Clin Invest*. 2005; 115(1):102–109.
27. Eberling JL, et al. Functional effects of AAV2-GDNF on the dopaminergic nigrostriatal pathway in parkinsonian rhesus monkeys. *Hum Gene Ther*. 2009; 20(5):511–518.
28. Ferri ALM, et al. Foxa1 and Foxa2 regulate multiple phases of midbrain dopaminergic neuron development in a dosage-dependent manner. *Development*. 2007;134(15):2761–2769.
29. McRitchie DA, Hardman CD, Halliday GM. Cytoarchitectural distribution of calcium binding proteins in midbrain dopaminergic regions of rats and humans. *J Comp Neurol*. 1996;364(1):121–150.
30. Bankiewicz KS, et al. Hemiparkinsonism in monkeys after unilateral internal carotid artery infusion of 1-methyl-4-phenyl-1,2,3,6-tetrahydropyridine (MPTP). *Life Sci*. 1986;39(1):7–16.
31. Frey S, et al. An MRI based average macaque monkey stereotaxic atlas and space (MNI monkey space). *Neuroimage*. 2011;55(4):1435–1442.
32. Clarke G, et al. A one-hit model of cell death in inherited neuronal degenerations. *Nature*. 2000; 406(6792):195–9.
33. Burbach JPH, Smidt MP. Molecular programming of stem cells into mesodiencephalic dopaminergic neurons. *Trends Neurosci*. 2006;29(11):601–603.
34. Lindvall O, et al. Grafts of fetal dopamine neurons survive and improve motor function in Parkinson's disease. *Science*. 1990;247(4942):574–577.
35. Freed CR, et al. Survival of implanted fetal dopamine cells and neurologic improvement 12 to 46 months after transplantation for Parkinson's disease. *N Engl J Med*. 1992;327(22):1549–1555.
36. Peschanski M, et al. Bilateral motor improvement and alteration of L-dopa effect in two patients with Parkinson's disease following intrastriatal transplantation of foetal ventral mesencephalon. *Brain*. 1994;117(pt 3):487–499.
37. Spencer DD, et al. Unilateral transplantation of human fetal mesencephalic tissue into the caudate nucleus of patients with Parkinson's disease. *N Engl J Med*. 1992;327(22):1541–1548.
38. Freed CR, et al. Transplantation of embryonic dopamine neurons for severe Parkinson's disease. *N Engl J Med*. 2001;344(10):710–719.
39. Olanow CW, et al. A double-blind controlled trial of bilateral fetal nigral transplantation in Parkinson's disease. *Ann Neurol*. 2003;54(3):403–414.
40. Li J-Y, Christophersen NS, Hall V, Soulet D, Brundin P. Critical issues of clinical human embryonic stem cell therapy for brain repair. *Trends in Neurosciences*. 2008;31(3):146–153.
41. Vinuela A, et al. Implanted reuptake-deficient or wild-type dopaminergic neurons improve ON L-dopa dyskinesias without OFF-dyskinesias in a rat model of Parkinson's disease. *Brain*. 2008; 131(pt 12):3361–3379.
42. Kittappa R, Chang WW, Awatramani RB, McKay RDG. The foxa2 gene controls the birth and spontaneous degeneration of dopamine neurons in old age. *PLoS Biol*. 2007;5(12):e325.
43. Cooper O, et al. Differentiation of human ES and Parkinson's disease iPS cells into ventral midbrain dopaminergic neurons requires a high activity form of SHH, FGF8a and specific regionalization by retinoic acid. *Mol Cell Neurosci*. 2010;45(3):258–266.
44. Cai J, et al. The role of Lmx1a in the differentiation of human embryonic stem cells into midbrain dopamine neurons in culture and after transplantation into a Parkinson's disease model. *Stem Cells*. 2009;27(1):220–229.
45. Hargus G, et al. Differentiated Parkinson patient-derived induced pluripotent stem cells grow in the adult rodent brain and reduce motor asymmetry in Parkinsonian rats. *Proc Natl Acad Sci USA*. 2010; 107(36):15921–15926.
46. Sonntag K-C, et al. Context-dependent neuronal differentiation and germ layer induction of Smad4$^{-/-}$ and Cripto$^{-/-}$ embryonic stem cells. *Mol Cell Neurosci*. 2005;28(3):417–429.
47. Kriks S, et al. Dopamine neurons derived from human ES cells efficiently engraft in animal models of Parkinson's disease. *Nature*. 2011;480(7378):547–551.
48. O'Keeffe FE, et al. Induction of A9 dopaminergic neurons from neural stem cells improves motor function in an animal model of Parkinson's disease. *Brain*. 2008;131(pt 3):630–641.
49. Kuan W-L, Lin R, Tyers P, Barker RA. The importance of A9 dopaminergic neurons in mediating the functional benefits of fetal ventral mesencephalon transplants and levodopa-induced dyskinesias. *Neurobiol Dis*. 2007;25(3):594–608.
50. De Camilli P, Miller PE, Navone F, Theurkauf WE, Vallee RB. Distribution of microtubule-associated protein 2 in the nervous system of the rat studied by immunofluorescence. *Neuroscience*. 1984; 11(4):817–846.
51. Xu H, et al. Transplantation of neuronal cells induced from human mesenchymal stem cells improves neurological functions after stroke without cell fusion. *J Neurosci Res*. 2010;88(16):3598–3609.
52. Freeman TB, Brundin P. Important aspects of surgical methodology for transplantation in Parkinson's disease. In: Brundin P, Olanow CW, eds. *Restorative Therapies in Parkinson's Disease*. New York, New York, USA: Springer; 2006:131–165.
53. Dubach M, et al. Primate neostriatal neurons containing tyrosine hydroxylase: immunohistochemical evidence. *Neurosci Lett*. 1987;75(2):205–210.
54. Guliás B, Halldin C. New PET radiopharmaceuticals beyond FDG for brain tumor imaging. *Q J Nucl Med Mol Imaging*. 2012;56(2):173–190.
55. Padma MV, et al. Functional imaging of a large demyelinating lesion. *J Clin Neurosci*. 2005;12(2):176–178.
56. Lewis DA, Sesack SR. Dopamine systems in the primate brain. In: Bloom FE, Björklund A, Hökfelt T. *The Primate Nervous System*. New York, New York, USA: Elsevier; 1997:263–375.
57. Kordower JH, Liu YT, Winn S, Emerich DF. Encapsulated PC12 cell transplants into hemiparkinsonian monkeys: a behavioral, neuroanatomical, and neurochemical analysis. *Cell Transplant*. 1995; 4(2):155–171.
58. Luthman J, Jonsson G. Effects of the parkinsonism-inducing neurotoxin MPTP and its metabolite MPP+ on sympathetic adrenergic nerves in mouse iris and atrium. *Med Biol*. 1986;64(2–3):95–102.
59. Kurlan R, Kim MH, Gash DM. Oral levodopa dose-response study in MPTP-induced hemiparkinsonian monkeys: assessment with a new rating scale for monkey parkinsonism. *Mov Disord*. 1991;6(2):111–118.
60. Jordan S, et al. 6-[18F]fluoro-L-m-tyrosine: metab-

olism, positron emission tomography kinetics, and 1-methyl-4-phenyl-1,2,3,6-tetrahydropyridine lesions in primates. *Brain Res.* 1997;750(1–2):264–276.
61. Emborg ME, et al. Age-related declines in nigral neuronal function correlate with motor impairments in rhesus monkeys. *J Comp Neurol.* 1998; 401(2):253–265.
62. Saiki H, Hayashi T, Takahashi R, Takahashi J. Objective and quantitative evaluation of motor function in a monkey model of Parkinson's disease. *J Neurosci Methods.* 2010;190(2):198–204.
63. Någren K, Müller L, Halldin C, Swahn CG, Lehikoinen P. Improved synthesis of some commonly used PET radioligands by the use of [11C] methyl triflate. *Nucl Med Biol.* 1995;22(2):235–239.
64. Herzog H, et al. NEMA NU2-2001 guided performance evaluation of four Siemens ECAT PET scanners. *IEEE Trans Nucl Sci.* 2004;51(5):2662–2669.
65. Gunn RN, Lammertsma AA, Hume SP, Cunningham VJ. Parametric imaging of ligand-receptor binding in PET using a simplified reference region model. *Neuroimage.* 1997;6(4):279–287.
66. Sturgeon C. Practice guidelines for tumor marker use in the clinic. *Clin Chem.* 2002;48(8):1151–1159.
67. Al-Sugair A, Coleman RE. Applications of PET in lung cancer. *Semin Nucl Med.* 1998;28(4):303–319.
68. Nichols TE, Holmes AP. Nonparametric permutation tests for functional neuroimaging: a primer with examples. *Hum Brain Mapp.* 2002;15(1):1–25.
69. Smith SM, Nichols TE. Threshold-free cluster enhancement: addressing problems of smoothing, threshold dependence and localisation in cluster inference. *Neuroimage.* 2009;44(1):83–98.

ヒト生体に内在する新たな多能性幹細胞　Muse細胞：細胞治療，予後の診断，創薬，病態解析への展開の可能性

東北大学大学院医学系研究科細胞組織学分野・人体構造学分野
出澤 真理
Mari DEZAWA

1.　はじめに

間葉系幹細胞は骨髄，脂肪，真皮，臍帯などに存在する組織幹細胞であり，腫瘍化の危険が低く安全性が高いこと，入手しやすい組織から得られることなどから，臨床試験が各国で精力的に進められている。栄養因子やサイトカインの産生による組織保護効果や抗炎症作用，アポトーシス調節作用をもたらすので様々な疾患を対象に移植が検討されており，また免疫抑制作用も持つことから，移植片対宿主病に対する臨床応用も進められている。

しかし，間葉系幹細胞にはこれらの作用の他に重要な作用がある。それは，胚葉を超えた幅広い分化と生体内での組織修復作用である。これらの作用は長らく科学的に議論されてきたが，間葉系幹細胞が様々な細胞種の混合から成り立っており，そのような幹細胞の本態が明らかにされてこなかったことや，生体内での組織修復効果の率が極めて低いなどの理由から実態がよくわかっていなかった。

我々の研究室ではヒトの間葉系組織や間葉系の培養細胞において，多能性を有するが腫瘍性を持たない新たなタイプの体性幹細胞Multiliniage-differentiating stress enduring (Muse) 細胞を見出した[1),2)]。この細胞は，成人の生体内に存在する多能性幹細胞であり，これまで間葉系幹細胞で見られてきた幅広い分化能や組織修復を説明すると考えられる。

■著者連絡先
東北大学大学院医学系研究科細胞組織学分野・人体構造学分野
（〒980-8575　宮城県仙台市青葉区星陵町2-1）
E-mail. mdezawa@med.tohoku.ac.jp

2.　生体内多能性幹細胞としてのMuse細胞

Muse細胞は間葉系幹細胞の一員であると同時に，多能性幹細胞としての振る舞いを見せる。このような特性はマーカーの発現にも見られ，間葉系マーカーCD29，CD105，CD90と同時に，未分化ヒトES細胞のマーカーstage specific embryonic antigen-3 (SSEA-3) のダブル陽性細胞，すなわち間葉系と多能性幹細胞の両方のマーカーを発現する細胞として同定される。

Muse細胞は1細胞レベルでの浮遊培養を行うと増殖を開始し，ヒトES細胞由来の胚葉体と酷似した細胞塊clusterを形成する[1)]。このclusterはアルカリフォスファターゼ反応に陽性を示し，Nanog，Sox2，Oct3/4などの多能性マーカーを発現する。さらに，この1細胞から形成された細胞塊をゲラチン上で培養するとsmooth muscle actin（平滑筋），desmin（骨格筋），alpha-fetoprotein（肝細胞），cytokeratin-7（胆道系細胞），neurofilament（神経）など三胚葉性の細胞へ自発的に分化する[1)]。このような自発的な三胚葉性の細胞への分化率は高くはなく，内胚葉性や外胚葉性の細胞が全体の3～4%，中胚葉性の細胞が10～15%であるが，一方，Muse細胞に特定の誘導をかけると90%以上の高い効率で神経，肝細胞，脂肪細胞，骨細胞などの目的とする細胞に分化させることが可能である。従ってMuse細胞からは効率の良いdirect reprogrammingが可能である。

Muse細胞は成人ヒトの皮膚，骨髄などの間葉系組織から採取可能である。生体の間葉系組織の場合，例えば骨髄液では，3,000個の骨髄単核球細胞のうち1細胞の割合で存在する[1),2)]。生体内でのMuse細胞の局在を組織学的に検討すると，真皮，脂肪組織や他の様々な臓器では結合組織内に孤立性・散在性に存在し，特定の組織構造との関連は

見られなかった[2]。また，市販の間葉系の培養細胞では，多少の増減はあるものの大体1%ないし数%程度の割合で含まれている。

3. Muse細胞は多能性であるが腫瘍性がない

腫瘍性増殖能に関わる因子の発現量を調べるとembryonic stem (ES) 細胞，induced pluripotent stem (iPS) 細胞は非常に高値を示すが，Muse細胞では体細胞とほぼ同じレベルで低い[2]。さらにヒト細胞への免疫拒絶を示さない免疫欠損マウス（SCIDマウス）の精巣への移植では，ヒトES細胞やiPS細胞は8～12週で奇形腫を形成するのに対し，ヒトMuse細胞では半年を経過しても奇形腫の形成は全く見られなかった[1]。間葉系幹細胞は腫瘍化の危険が低く，すでにヒトに移植されている細胞であり，Muse細胞はその間葉系幹細胞の一部であることと併せて考えると，もともと腫瘍化の危険は低いと思われる。

4. Muse細胞は生体に投与されると組織修復機能をもたらす

ヒト細胞を拒絶しない免疫欠損マウスを用いて劇症肝炎，筋変性，脊髄損傷，皮膚損傷などの様々なモデルを作製し，GFPで標識したヒトMuse細胞を尾静脈から投与すると（ただし皮膚損傷の場合は局所注入を行った），移植4週後でMuse細胞は傷害部位に生着し，肝細胞，筋細胞，神経細胞，角化細胞にそれぞれ分化することが確認されている[1]。

SCIDマウスの腹腔に四塩化炭素を投与して作製した劇症肝炎モデルでは，尾静脈から投与したGFP陽性のヒトMuse細胞が肝臓の傷害部位に経血管的に生着しており，さらに，生着した細胞の約90%近くがヒトアルブミンやヒトアンチトリプシンをマウス肝臓内発現することが確認された。マウスの末梢血を採取しWestern blotで解析するとヒトアルブミンが検出されたことから，移植されたヒトのMuse細胞がマウスの肝臓内に生着し，ヒト肝細胞として分化し，さらにヒトのアルブミンを血中に放出することのできる機能的細胞になっていたということを示唆する[1]。

同様に，筋変性モデルに生着したヒトMuse細胞はヒトのジストロフィンを，損傷脊髄ではneurofilamentを，損傷皮膚ではcytokeratin 14を発現していた[1]。このように，投与されたヒトMuse細胞は生体内で損傷部位を認識して生着し，機能的な細胞に分化すること，さらに三胚葉性の細胞に生体内でそれぞれ分化することが示された。

一方Muse細胞を除いたヒト間葉系幹細胞，すなわち非Muse細胞群を同様の方法で生体に投与しても，Muse細胞で見られたような損傷組織への生着や各組織の細胞への分化は観察されない[1]。従って，Muse細胞は損傷部位を認識し，組織を構成する細胞となりうる組織修復機能を持つが，Muse細胞以外の間葉系幹細胞にはこのような機能が備わっていない，すなわち間葉系幹細胞移植においてこれまで見られてきた組織再生，組織修復はMuse細胞が担っていると考えられる。

Muse細胞の特性をまとめると，

- 遺伝子導入などの人工的な操作なしに，ヒト生体から直接得られる多能性幹細胞。三胚葉性の多様な細胞に分化できる。
- 入手しやすい皮膚，骨髄，脂肪や市販の線維芽細胞などから採取可能である。
- 腫瘍化の危険性が低い。
- 骨髄移植の0.03%，間葉系幹細胞移植の数%に相当。すでに移植されている細胞の一部であり，安全性の見通しが高い。
- 培養では線維芽細胞と同程度の増殖力を持ち，脂肪や骨髄から細胞数確保が可能。
- 生体内にそのまま投与すると組織修復をもたらす。

などの特徴に集約される。

5. 再生医療におけるMuse細胞の可能性と戦略

間葉系幹細胞は組織保護や修復に効果があるとされ，臨床応用も進められているが，特に再生効果・組織修復作用に関しては明快な科学的根拠が提示されてこなかった。そのような中で，三胚葉性の細胞への幅広い分化能力を有する多能性のMuse細胞が間葉系幹細胞の中から同定され，さらにはこの細胞が再生効果，組織修復効果を担っているということが明らかになったことには再生医学において意義がある。これまで雑駁な間葉系幹細胞をそのまま生体に投与する形で臨床試験などが行われているが，その中に含まれるMuse細胞を精製する，あるいは比率を上げることによって組織修復効率の向上や有効性の高い再生医療への応用が期待される。ただし，Muse細胞以外の間葉系細胞が必要であるのか不要なのか，この点は慎重な判断が必要と思われる。疾患によっては急性の炎症，組織破壊など複合的な要因が絡み合っている場合がある。このような「場」にMuse細胞だけを投与するよりも，抗炎症，抗アポトーシス作用を持ち組織保護をもたらす非Muse細胞が一定程度存在するほうが，Muse細胞自身の生着，生存が上がり，結果として有効な組織再生につながる可能性がある。Muse細胞をどのように有効活用するかは今後の大きな課題である。

本稿の著者には規定されたCOIはない。

文　献

1) Kuroda Y, Kitada M, Wakao S, et al: Unique multipotent cells in adult human mesenchymal cell populations. Proc Natl Acad Sci USA **107**: 8639-43, 2010
2) Wakao S, Kitada M, Kuroda Y, et al: Multilineage-differentiating stress-enduring (Muse) cells are a primary source of induced pluripotent stem cells in human fibroblasts. Proc Natl Acad Sci USA **108**: 9875-80, 2011

Pathology International

Pathology International 2013; **63**: 305–310 doi:10.1111/pin.12064

Original Article

Quantification of collagen and elastic fibers using whole-slide images of liver biopsy specimens

Tokiya Abe,[1] Akinori Hashiguchi,[1] Ken Yamazaki,[1] Hirotoshi Ebinuma,[2,3] Hidetsugu Saito,[2,3] Hiromitsu Kumada,[4] Namiki Izumi,[5] Naohiko Masaki[6] and Michiie Sakamoto[1]

Departments of [1]Pathology and [2]Internal Medicine, School of Medicine, and [3]Faculty of Pharmacy, Keio University, [4]Department of Gastroenterology, Toranomon Hospital, [5]Department of Gastroenterology and Hepatology, Musashino Red Cross Hospital, Tokyo and [6]The Research Center for Hepatitis and Immunology, National Center for Global Health and Medicine, Chiba, Japan

Histological evaluation of fibrosis after a liver biopsy is crucial for evaluating the pathology of patients with chronic liver disease. Previous studies have reported quantitative analyses of fibrosis using images of collagen-stained sections. However, analysis of these studies requires manual selection of the region of interest. In addition, the quantification of elastic fibers is not considered. The present study was conducted in order to measure both the collagen and elastic fiber area ratios using Elastica van Gieson-stained whole-slide images (WSIs) of liver biopsy specimens. High-resolution WSIs provide precise color classification, enabling accurate detection of even fine collagen and elastic fibers. To minimize the influence of pre-existing fibrous tissue, median area ratios of the collagen and elastic fibers were independently calculated from the image tiles of the WSIs. These median area ratios were highly concordant with area ratios after the pre-existing fibrous tissues were manually trimmed from the WSI. Further, these median area ratios were correlated with liver stiffness as measured by transient elastography (collagen: $r = 0.73$ [$P < 0.01$], elastic: $r = 0.53$ [$P < 0.01$]). Our approach to quantifying liver fibrosis will serve as an effective tool to evaluate liver diseases in routine practice.

Key words: collagen, computer-assisted image analysis, elastin, elastography, liver fibrosis, whole-slide image

Evaluation of liver fibrosis in patients with chronic liver disease is crucial for understanding the disease state, predicting prognosis and selecting the appropriate treatment.[1,2] Although the efficacy of biochemical methods[3–6] and transient elastography for measuring liver stiffness[7] has been demonstrated, histopathological evaluation of liver biopsy specimens remains the gold standard. At present, histopathological evaluation of fibrosis using liver biopsy specimens is performed by a pathologist who stages specimens by identifying the location, degree and pattern of fibrosis, presence of architectural distortion, and regenerative nodule formation. This staging is completely dependent on the experience of the observer, and there is intra- as well as inter-individual variation in this respect.[1] To overcome these issues, quantification by imaging analysis has been suggested for evaluating the degree of liver fibrosis.[8–17] In these studies, collagen fibers were extracted from the histological image of the liver biopsy specimen, and the area occupied by the fibers relative to the area of the entire tissue specimen was quantified as a ratio. However, most of the proposed quantification methods still need an observer to define the region of interest or trim pre-existing fibrous tissue such as skin, muscle, or a large blood vessel.[8–14] An increase in collagen deposition is involved in the progression of liver fibrosis. Deposition of elastic fibers is also reportedly increased, particularly in late stages of the disease.[18–21] Thus, evaluation of elastic as well as collagen fiber deposition is crucial for the accurate evaluation of fibrosis progression; however, to our knowledge, no method that simultaneously quantifies both fibers has been reported to date.

The whole-slide imaging system, which is popular in telepathology and education, enables an entire tissue section to be digitized at a high resolution within minutes and saved as a whole-slide image (WSI).[22–24] Once the WSI is stored as digital data, it is easy to obtain individual pixel color values, and WSIs can be used for several applications including morphometrical analysis.[25–28] The purpose of this study is to develop an effective method to quantify liver fibrosis using

Correspondence: Michiie Sakamoto, MD, PhD, Department of Pathology, School of Medicine, Keio University, 35 Shinanomachi, Shinjuku-ku, Tokyo 160-8582, Japan. Email: msakamot@z5.keio.jp

Received 24 January 2013. Accepted for publication 2 May 2013.

the WSIs of liver biopsy specimens. We established a method that simultaneously quantifies the collagen and elastic fiber area ratios in Elastica van Gieson (EVG)-stained liver biopsy tissue specimens. Further, the area ratios were compared with liver stiffness as measured by transient elastography. This method of quantifying liver fibrosis using WSIs may become important in the future as a technique for assisting with pathological diagnosis.

METHODS

Samples

Liver biopsy specimens were collected from 38 chronic viral hepatitis patients (37 with chronic hepatitis C virus, and one with chronic hepatitis B virus) from four medical facilities. After obtaining the informed consent, we measured the liver stiffness by using FibroScan (Echo-Sens, Paris, France). The stiffness of the right lobe of the liver was measured by placing a probe tip into the intercostal space at a depth of 2.5–6 cm from the skin surface. Liver stiffness was measured 10 times, and the median value of these 10 measurements was used for each patient.

EVG staining

The liver biopsy specimens were formalin-fixed and paraffin-embedded. The specimens were then sliced to a thickness of 3 μm and stained with EVG. A WSI of each specimen was acquired using the NanoZoomer 2.0HT (Hamamatsu Photonics K.K., Hamamatsu, Japan) at a × 20 objective lens equivalent to 0.46 μm/pixel.

Quantification of fibrosis using WSI analysis

The WSI pixels were classified into five classes corresponding to four tissue components: collagen fibers, elastic fibers, nucleus, cytoplasm, and one non-tissue component (i.e. glass slide). The training data points, which were extracted from the portal and periportal areas in the WSI, were sampled for at least 30 points for each class. The color distributions of the five classes were analyzed in RGB color space, wherein the color analyses were done for all specimens. Subsequently, a quadratic discriminant function based on the color distribution[29] was applied in order to label each WSI pixel appropriately.

The area ratio of each tissue component is the sum of pixels for each tissue component divided by the total number of pixels of the four tissue components. The median area ratios of collagen and elastic fibers were also calculated. An image-processing program was developed using MATLAB (The MathWorks, Inc., Natick, MA, USA) for image analysis.

Statistical analysis

Relationships between measurement values were analyzed using the Spearman's rank correlation coefficient test. All *P*-values were two-tailed, and values less than 0.05 were considered statistically significant. Analyses were carried out using SPSS software (version 19.0; SPSS Inc., Chicago, IL, USA).

RESULTS

The evaluated liver biopsy specimens had an average length of 16.3 mm (SD = 3.2 mm) and an average width of 1.0 mm (SD = 0.3 mm). This is equivalent to an average of 77 mega-pixels (SD = 36 mega-pixels) in WSIs. The time required for analysis was approximately 6.3 min (SD = 3.3 min) per biopsy specimen.

Color classification of EVG-stained tissue specimens

The training data points for five classes were from the portal and periportal areas on the WSI of EVG-stained liver biopsy specimens (Fig. 1a). The extracted training data points were plotted in RGB color space (Fig. 1b). Five classes of the data points in all liver biopsy specimens were individually distinguishable in the three-dimensional color space. The composition of the color distribution of the five classes was different among the biopsy specimens, therefore, the quadratic discriminant function was designed based on the training data points in each liver biopsy specimen and applied to determine the color classification of the pixels. As a result, every pixel on the WSIs of all liver biopsy specimens was successfully labeled in the appropriate classes (Figs S1,S2). Figure 2 shows that even fine collagen and elastic fibers could be extracted from portal and periportal areas.

Measurements of the area ratios of tissue components on WSIs

The area ratio of each tissue component could be calculated from the labeled pixels. The average area ratios of collagen, elastic fibers, nucleus and cytoplasm in all biopsy specimens were 11.3% (SD = 5.1%), 3.8% (SD = 2.7%), 11.8% (SD = 5.0%) and 73.1% (SD = 8.7%), respectively. Representative WSIs and classification results of liver biopsy specimens with mild fibrosis and severe fibrosis are shown in

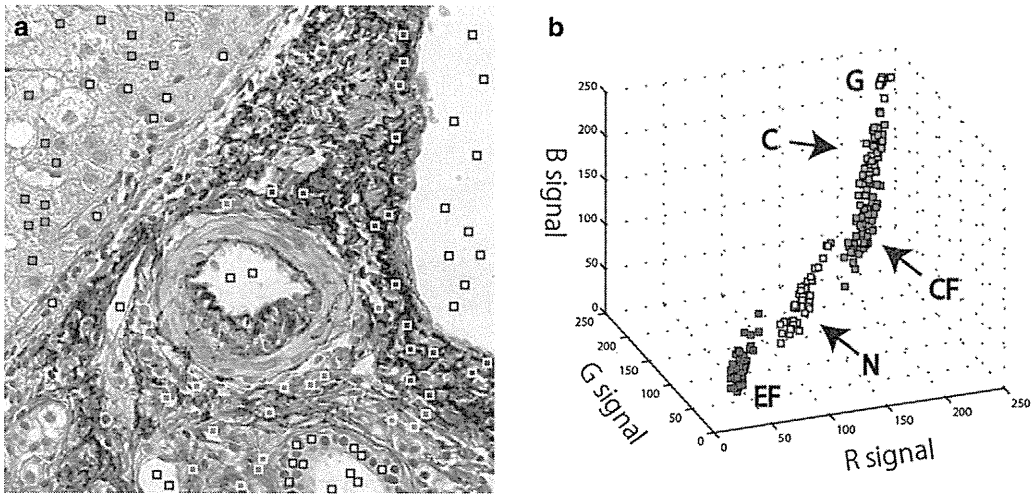

Figure 1 Sampling and color distribution. (**a**) Colored squares indicate training data points for five classes in the portal and periportal area (250 × 250 μm^2). (**b**) Color distribution of the data points in RGB color space. Each color represents a class: collagen fiber (CF), red; elastic fibers (EF), blue; cell nuclei (N), yellow; cytoplasm (C), green; glass slide (G), white.

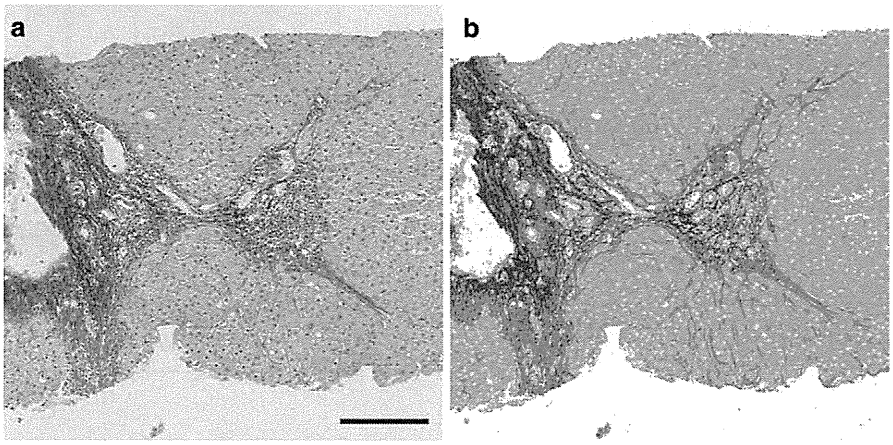

Figure 2 Color image and classification result in the portal and periportal areas (1 × 1 mm^2). In the color classification result, collagen fibers, elastic fibers, nuclei, cytoplasm, and glass slide were red, blue, yellow, green, and white, respectively. Scale bar, 0.2 mm.

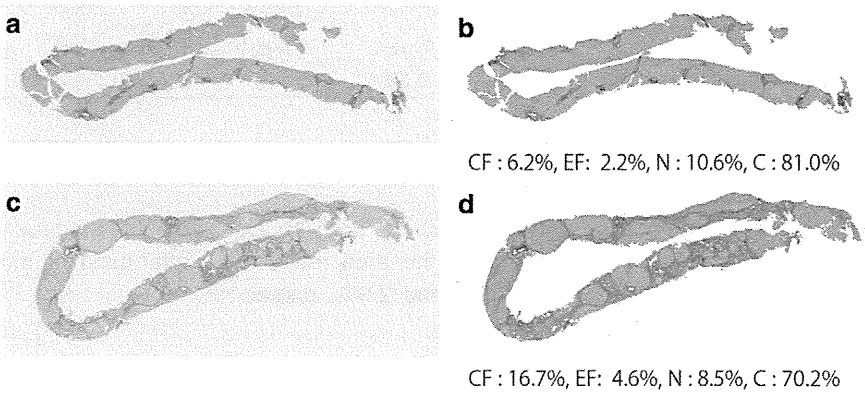

Figure 3 Measurements of area ratio on the whole-slide image. Representative whole slide images (WSIs) and classification results of liver biopsy specimen with mild fibrosis (**a,b**) and with severe fibrosis (**c,d**). The percentage indicates area ratio of each tissue component.

Figure 3a–d. The area ratios of collagen, elastic fibers, nucleus, and cytoplasm were 6.2%, 2.2%, 10.6%, and 81.0%, respectively, for mild fibrosis. The area ratios for severe fibrosis were 16.7%, 4.6%, 8.5%, and 70.2%, respectively. The area ratios of collagen as well elastic fibers were higher for patients with severe fibrosis than for those with mild fibrosis.

Median area ratios of collagen and elastic fibers

Previous papers reported that pre-existing fibrous tissue, such as muscle and large blood vessels (enclosed by the dotted line in Fig. 4a), should be trimmed from the WSI prior to implementing image analysis.[8,9] The measurements show that without trimming the pre-existing fibrous tissue,

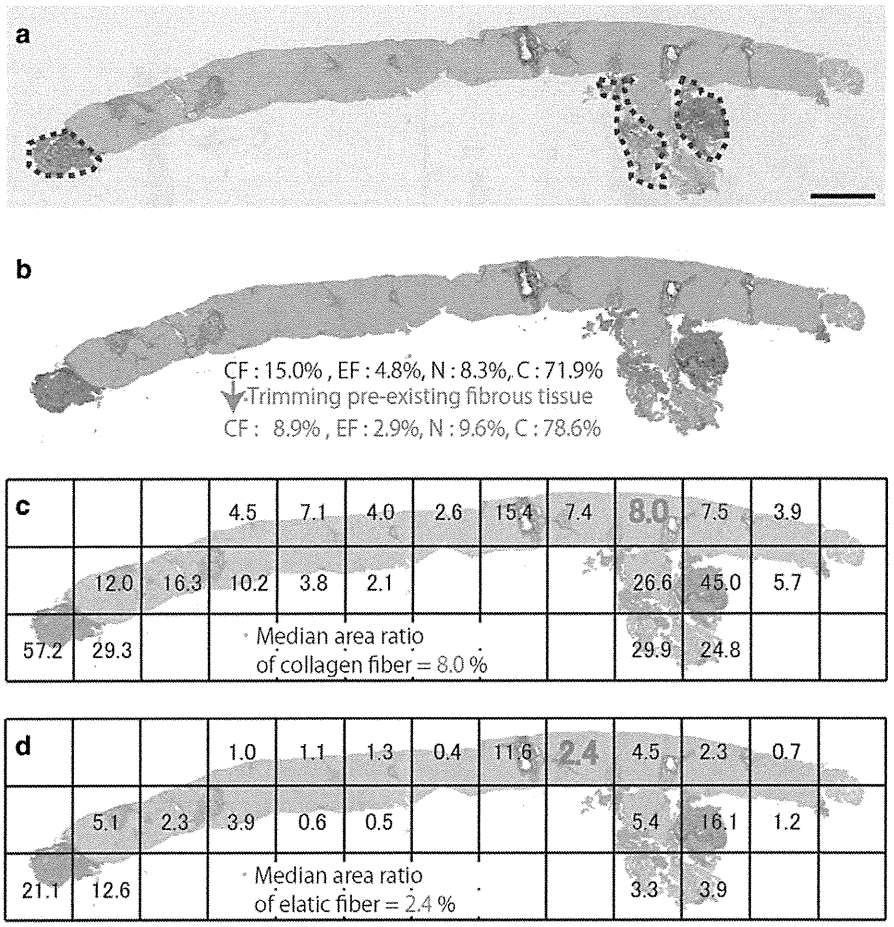

Figure 4 Median area ratios of collagen and elastic fibers. (**a,b**) Whole-slide image (WSI) and classification result of the liver biopsy specimen with mild fibrosis. (**c,d**) Median area ratios of collagen and elastic fibers, respectively, when the classification result was divided into 1×1 mm^2. Black numbers indicate area ratios of each fiber for any tiles where the tissue area occupied at least 20% of the tile area. The red number was the median area ratio of each fiber. Scale bar, 1 mm.

Table 1 Correlation between the median area ratio and area ratio after trimming the pre-existing fibrous tissue from the whole slide image

Tile size (mm^2)	0.01^2	0.25^2	0.50^2	0.75^2	1.00^2	1.25^2	1.50^2
Spearman's rank correlation coefficient							
Collagen fiber	0.79**	0.94**	0.98**	0.97**	0.98**	0.95**	0.93**
Elastic fiber	0.59**	0.87**	0.93**	0.93**	0.95**	0.92**	0.88**

**$P < 0.01$.

the area ratios of collagen and elastic fibers were 15.0% and 4.8%, respectively. After trimming, the area ratios of collagen and elastic fibers were 8.9% and 2.9%, respectively (Fig. 4b).

We then calculated the median area ratios of collagen and elastic fibers from the image tiles of WSI (Fig. 4c,d). The WSI was divided into small tiles of 1×1 mm^2. Then area ratios of each fiber on any tile, where the tissue area occupied at least 20% of the tile area, was calculated. The median area ratios of collagen and elastic fibers were determined as 8.0% (Fig. 4c) and 2.4% (Fig. 4d), respectively.

In order to determine the appropriate tile size, correlation between the median area ratios in other tile sizes and the area ratio after trimming were evaluated for all 38 liver biopsy specimens (Table 1). When the tile size was 1×1 mm^2, the median area ratios of the fibers correlated with the area ratio after trimming most strongly.

Relationship between the area ratio of fiber and liver stiffness

Correlation between the median area ratio of each fiber and liver stiffness measured by transient elastography was evaluated (Fig. 5a,b). Liver stiffness correlated well with the median area ratios of both types of fibers using a tile size of 1×1 mm^2 (collagen fiber: $r = 0.73$ [$P < 0.01$]; elastic fiber: $r = 0.53$ [$P < 0.01$]), as well as the area ratios after trimming pre-existing fibrous tissue off from WSI (collagen fiber: $r = 0.73$ [$P < 0.01$], elastic fiber: $r = 0.51$ [$P < 0.01$]). Liver

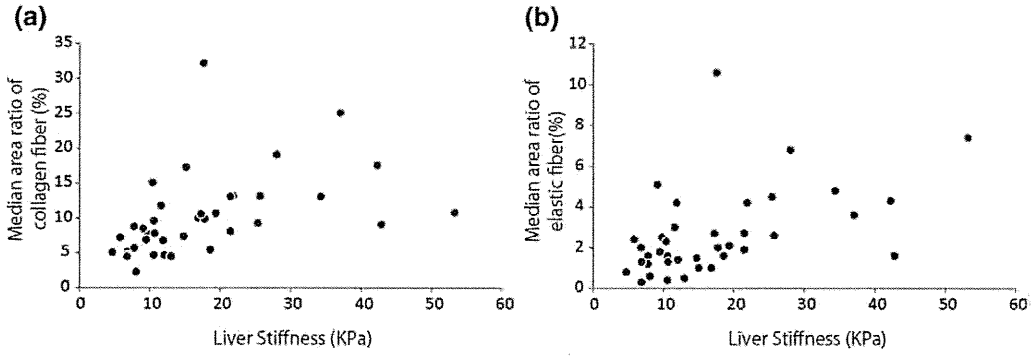

Figure 5 Scatter plot of liver stiffness by transient elastography versus median area ratios of (**a**) collagen and (**b**) elastic fibers. The tile size was 1×1 mm^2 when calculating the median area ratios of both fibers.

stiffness showed better correlation with the median area ratios of both fibers than with the area ratios including pre-existing fibrous tissue (collagen fiber: $r = 0.62$ [$P < 0.01$], elastic fiber: $r = 0.44$ [$P < 0.01$]).

DISCUSSION

Our color classification technique successfully labeled the WSI pixels of EVG-stained liver biopsy specimens in the appropriate classes (collagen, elastic fibers, nucleus, cytoplasm, and glass slide). Even fine collagen and elastic fibers, associated with chronic hepatitis, were accurately detected. Our results suggest that the precise recognition of tissue components in WSIs could identify not only portal fibrosis in patients with chronic viral hepatitis, but also fine pericellular fibrosis in those with alcoholic and non-alcoholic fatty liver diseases.

Pre-existing fibrous tissue such as skin, muscle and large blood vessel affects the accuracy of liver fibrosis measurements.[8] Previous studies have reported that the area ratio of collagen fiber was calculated after trimming pre-existing fibrous tissue from WSI.[8,9] Our study indicates that the trimming step could be avoided by calculating the median area ratios of collagen and elastic fibers from the image tiles of WSI. This approach can minimize the human factor and serve to establish an objective and automated quantification method. This type of image processing is one of the advantages of WSI analysis. We believe that more beneficial and useful algorithms will be developed in the near future.

Liver stiffness measured by transient elastography has been reported to correlate with the liver fibrosis stages.[7] Our results show that liver stiffness had a better correlation with the median area ratios of fibers than with the area ratios of fibers, including pre-existing fibrous tissue. This result suggests that the median area ratio of each fiber increases the correlation with liver stiffness and reflects the progression of liver fibrosis quantitatively. The liver stiffness, especially, correlated better with the median area ratio of collagen fiber than with the median area ratio of elastic fiber, probably due to an increase in elastic fiber in the late stages of the disease.[19–21] It is also possible that liver stiffness may relate to the width or density of fibrous septa.[30] However, we need to integrate other algorithms or densitometric method in order to measure those parameters and illuminate their relationships. The quantification of collagen and elastic fibers in a large number of cases would contribute to the understanding of the mechanism of fibrosis progression associated with chronic liver disease with different etiology, and would help to evaluate clinical usefulness.

In conclusion, a method for simultaneously quantifying collagen and elastic fibers was developed using WSIs of EVG-stained liver biopsy specimens. Median area ratios of collagen and elastic fibers obtained from the image tiles of WSIs were found to be correlated with liver stiffness measured by transient elastography. This enabled more accurate quantification of liver fibrosis than the area ratio of each fiber, including pre-existing fibrous tissue. Our approach of quantifying liver fibrosis will serve as a useful tool to effectively evaluate liver diseases in routine practice.

ACKNOWLEDGMENTS

This study was supported by the New Energy and Industrial Technology Development Organization (NEDO). The authors thank K. Effendi, M. Iwata, M. Takeichi, Y. Nagafuji, and Y. Hashimoto for technical assistance.

REFERENCES

1 The French METAVIR Cooperative Study Group. Intraobserver and interobserver variations in liver biopsy interpretation in patients with chronic hepatitis C. *Hepatology* 1994; **20**: 15–20.
2 Desmet VJ, Knodell RG, Ishak KG *et al.* Formulation and application of a numerical scoring system for assessing histological activity in asymptomatic chronic active hepatitis [Hepatology 1981; 1: 431–435]. *J Hepatol* 2003; **38**: 382–6.
3 Koda M, Matunaga Y, Kawakami M, Kishimoto Y, Suou T, Murawaki Y. FibroIndex, a practical index for predicting significant fibrosis in patients with chronic hepatitis C. *Hepatology* 2007; **45**: 297–306.

4 Forns X, Ampurdanes S, Llovet JM *et al.* Identification of chronic hepatitis C patients without hepatic fibrosis by a simple predictive model. *Hepatology* 2002; **36**: 986–92.
5 Wai CT, Greenson JK, Fontana RJ *et al.* A simple noninvasive index can predict both significant fibrosis and cirrhosis in patients with chronic hepatitis C. *Hepatology* 2003; **38**: 518–26.
6 Ngo Y, Munteanu M, Messous D *et al.* A prospective analysis of the prognostic value of biomarkers (FibroTest) in patients with chronic hepatitis C. *Clin Chem* 2006; **52**: 1887–96.
7 Ebinuma H, Saito H, Komuta M *et al.* Evaluation of liver fibrosis by transient elastography using acoustic radiation force impulse: Comparison with Fibroscan ®. *J Gastroenterol* 2011; **46**: 1238–48.
8 Standish RA, Cholongitas E, Dhillon A, Burroughs AK, Dhillon AP. An appraisal of the histopathological assessment of liver fibrosis. *Gut* 2006; **55**: 569–78.
9 Calvaruso V, Burroughs AK, Standish R *et al.* Computer-assisted image analysis of liver collagen: Relationship to Ishak scoring and hepatic venous pressure gradient. *Hepatology* 2009; **49**: 1236–44.
10 Goodman ZD, Becker RL Jr, Pockros PJ, Afdhal NH. Progression of fibrosis in advanced chronic hepatitis C: Evaluation by morphometric image analysis. *Hepatology* 2007; **45**: 886–94.
11 Goodman ZD, Stoddard AM, Bonkovsky HL *et al.* HALT-C Trial Group. Fibrosis progression in chronic hepatitis C: Morphometric image analysis in the HALT-C trial. *Hepatology* 2009; **50**: 1738–49.
12 Lazzarini AL, Levine RA, Ploutz-Snyder RJ, Sanderson SO. Advances in digital quantification technique enhance discrimination between mild and advanced liver fibrosis in chronic hepatitis C. *Liver Int* 2005; **25**: 1142–9.
13 McHutchison J, Goodman Z, Patel K *et al.*; Farglitizar Study Investigators. Farglitazar lacks antifibrotic activity in patients with chronic hepatitis C infection. *Gastroenterology* 2010; **138**: 1365–73. 1673 e1–2.
14 O'Brien MJ, Keating NM, Elderiny S *et al.* An assessment of digital image analysis to measure fibrosis in liver biopsy specimens of patients with chronic hepatitis C. *Am J Clin Pathol* 2000; **114**: 712–18.
15 Wright M, Thursz M, Pullen R, Thomas H, Goldin R. Quantitative versus morphological assessment of liver fibrosis: Semi-quantitative scores are more robust than digital image fibrosis area estimation. *Liver Int* 2003; **23**: 28–34.
16 Masseroli M, Caballero T, O'Valle F, Del Moral RM, Perez-Milena A, Del Moral RG. Automatic quantification of liver fibrosis: Design and validation of a new image analysis method: Comparison with semi-quantitative indexes of fibrosis. *J Hepatol* 2000; **32**: 453–64.
17 Hui AY, Liew CT, Go MY *et al.* Quantitative assessment of fibrosis in liver biopsies from patients with chronic hepatitis B. *Liver Int* 2004; **24**: 611–18.
18 Shikata T, Skai T. Elastogenesis in the liver. *Acta Pathol Jpn* 1974; **24**: 21–31.
19 Scheuer PJ, Maggi G. Hepatic fibrosis and collapse: Histological distinction by orecin staining. *Histopathology* 1980; **4**: 487–90.
20 Thung SN, Gerber MA. The formation of elastic fibers in livers with massive hepatic necrosis. *Arch Pathol Lab Med* 1982; **106**: 468–9.
21 Bedossa P, Lemaigre G, Paraf F, Martin E. Deposition and remodelling of elastic fibres in chronic hepatitis. *Virchows Arch A Pathol Anat Histopathol* 1990; **417**: 159–62.
22 Gilbertson JR, Ho J, Anthony L, Jukic DM, Yagi Y, Parwani AV. Primary histologic diagnosis using automated whole slide imaging: A validation study. *BMC Clin Pathol* 2006; **6**: 4.
23 Glatz-Krieger K, Glatz D, Mihatsch MJ. Virtual slides: High-quality demand, physical limitations, and affordability. *Hum Pathol* 2003; **34**: 968–74.
24 Weinstein RS, Graham AR, Richter LC *et al.* Overview of telepathology, virtual microscopy, and whole slide imaging: Prospects for the future. *Hum Pathol* 2009; **40**: 1057–69.
25 Diamond J, Anderson NH, Bartels PH, Montironi R, Hamilton PW. The use of morphological characteristics and texture analysis in the identification of tissue composition in prostatic neoplasia. *Hum Pathol* 2004; **35**: 1121–31.
26 Hashiguchi A, Hashimoto Y, Suzuki H, Sakamoto M. Using immunofluorescent digital slide technology to quantify protein expression in archival paraffin-embedded tissue sections. *Pathol Int* 2010; **60**: 720–25.
27 Puppa G, Risio M, Sheahan K *et al.* Standardization of whole slide image morphologic assessment with definition of a new application: Digital slide dynamic morphometry. *J Pathol Inform* 2011; **2**: 48.
28 Sertel O, Kong J, Shimada H, Catalyurek UV, Saltz JH, Gurcan MN. Computer-aided prognosis of neuroblastoma on whole-slide images: Classification of stromal development. *Pattern Recognit* 2009; **42**: 1093–103.
29 Gonzalez RC, Woods RE. Object recognition. In: Gonzalez RC, Woods RE, eds. *Digital Image Processing*, 3rd edn. Upper Saddle River, NJ: Pearson Prentice Hall, 2010; 896–9.
30 Zhang YG, Wang BE, Wang TL, Ou XJ. Assessment of hepatic fibrosis by transient elastography in patients with chronic hepatitis B. *Pathol Int* 2010; **60**: 284–90.

SUPPORTING INFORMATION

Additional Supporting Information may be found in the online version of this article at the publisher's web-site:

Figure S1 Whole slide images (WSIs) of liver biopsies from 38 chronic viral hepatitis patients.

Figure S2 Color classification results for WSIs.

EXPERIMENTAL CELL RESEARCH 319 (2013) 113–121

Available online at www.sciencedirect.com

SciVerse ScienceDirect

journal homepage: www.elsevier.com/locate/yexcr

Research Article

Leucine-rich repeat-containing G protein-coupled receptor 5 regulates epithelial cell phenotype and survival of hepatocellular carcinoma cells

Mariko Fukuma[a], *Keiji Tanese*[b], *Kathryn Effendi*[a], *Ken Yamazaki*[a], *Yohei Masugi*[a], *Mariko Suda*[a], *Michiie Sakamoto*[a,*]

[a]*Department of pathology, Keio University School of Medicine, Shinjuku-ku, Tokyo 160-8582, Japan*
[b]*Department of dermatology, Keio University School of Medicine, Shinjuku-ku, Tokyo 160–8582, Japan*

ARTICLE INFORMATION

Article Chronology:
Received 28 June 2012
Received in revised form
11 October 2012
Accepted 26 October 2012
Available online 2 November 2012

Keywords:
LGR5
GPR49
Hepatocellular carcinoma
Morphology
Motility

ABSTRACT

The leucine-rich repeat containing G protein-coupled receptor 5 (LGR5), also known as GPR49, is a seven-transmembrane receptor that is expressed in stem cells of the intestinal crypts and hair follicles of mice. LGR5 is overexpressed in some types of human cancer, and is one of the target genes of the Wnt signaling pathway. To explore the function of LGR5 in cancer cells, stable hepatocellular carcinoma (HCC) cell lines expressing FLAG-tagged LGR5 were established. Overexpression of LGR5 resulted in changes in cell shape from an extended flat (mesenchymal) phenotype to a round aggregated (stem cell-like) phenotype. Cells transfected with LGR5 showed higher colony forming activity, and were more resistant to a cytotoxic drug than cells transfected with empty vector. Overexpression of LGR5 inhibited cell motility. LGR5-transfected cells formed nodule type tumors in the livers of immunodeficient mice, whereas empty vector-transfected cells formed more invasive tumors. Down-regulation of LGR5 changed the morphology of HCC cells from the aggregated phenotype to an extended spindle phenotype, and cell motility was increased. This is the first study reporting the functional role of LGR5 in the biology of HCC cells, and the results suggest that aberrant expression of LGR5 regulates epithelial cell phenotype and survival.

Introduction

The leucine-rich repeat-containing G protein-coupled receptor 5 (LGR5), aliases G protein-coupled receptor 49 (GPR49), FEX, GPR67, GRP49, HG38, MGC117008, is structurally related to members of the glycoprotein hormone receptor family. In mice, deficiency of this gene causes neonatal lethality as a result of ankyloglossia [1]. LGR5 deficiency also induces premature differentiation of Paneth cells [2]. Recent studies from the Netherlands showed that in a mouse model, the homolog of this gene was a marker of intestinal and hair follicle stem cells. Introduction of an adenomatous polyposis coli (APC) mutation into LGR5-expressing cells increased the incidence of adenomas in mouse intestinal epithelial cells [3–5].

*Correspondence to: Department of pathology, Keio University School of Medicine, 35 Shinanomachi, Shinjuku-ku, Tokyo 160-8582, Japan. Fax: +81 3 3353 3290.
E-mail address: msakamot@z5.keio.jp (M. Sakamoto).

0014-4827/$ - see front matter © 2012 Elsevier Inc. All rights reserved.
http://dx.doi.org/10.1016/j.yexcr.2012.10.011

LGR5 has been reported to be upregulated in several tumors. We have previously shown that expression of LGR5 in the noncancerous liver was very low, however LGR5 is frequently overexpressed in hepatocellular carcinoma (HCC) with β-catenin mutations [6]. Although mutations of β-catenin are found in nearly 40% of HCC, the LGR5 has not been reported as the marker of hepatocyte, nor mentioned as a marker gene for liver regeneration. LGR5 also has been identified as a gene responsible to promote cell proliferation and tumor formation in basal cell carcinoma (BCC), a common malignant tumor of the skin [7]. High levels of LGR5 expression were also reported in colon and ovarian carcinomas [8], and we have shown that a high level of LGR5 expression in colorectal cancer was significantly correlated with tumor stage [9]. One study using colorectal cancer cell lines showed that suppression of LGR5 expression enhances tumorigenesis and is linked to a more mesenchymal phenotype [10].

There are some evidences suggest that LGR5 is a downstream target gene of Wnt signaling pathway [2,6,11,12]. The Wnt signaling pathway comprises a vast number of protein interactions and plays a critical role in morphogenesis and tumorigenesis. To date, three main pathways related to Wnt signaling have been identified: the β-catenin-dependent, planar cell polarity, and Wnt/Ca^{2+} pathways [13]. The β-catenin-dependent pathway, otherwise known as the canonical pathway, has been the most intensively studied. Mutations or deletions in AXN1/2 or APC genes inhibit the phosphorylating activity of GSK-3β, thereby stabilizing cytoplasmic β-catenin, and provoking aberrant cellular gene expression. Mutations at sites that affect β-catenin phosphorylation also cause cytoplasmic accumulation of β-catenin and lead to dysregulation of the pathway. Recently, LGR5 was reported to be a receptor of R-spondins which were known to be a potent family protein mediating Wnt/β-catenin and Wnt/PCP signaling [11,12,14]. Acquirement of stem cell-like properties in various tumors have greatly increased the possible role of these cells in tumorigenesis [15,16]. Upregulation of LGR5 in several tumors with increased Wnt signaling pathway suggests the possible role of LGR5 gene in oncogenesis and morphogenesis [6–9]. However, the functional role of LGR5 in tumor cells is still poorly understood. In this study, we aimed to analyze the function of LGR5 in hepatocellular carcinoma cells.

Materials and methods

Cell culture and chemicals

Cells were cultured in RPMI 1640 supplemented with 10% fetal bovine serum, 100 U/ml of penicillin and 100 μg/ml of streptomycin [6,9]. HepG2 containing a deletion of exon 3 of the β-catenin gene and PLC/PRF/5 containing a deletion of exon 4 of the AXIN1 were used as cell lines with activated Wnt signaling and high levels of LGR5 mRNA[17]. KYN2 cells were used as a cell line with low expression of LGR5 mRNA [6,9].

Plasmids, transfection, and establishment of stable transfectants

A FLAG-tagged LGR5 expression vector (LGR5-FL) was constructed by inserting the full-length coding cDNA for human LGR5 (RZPD, Berlin, Germany) into the Bgl II site of p3XFLAG-CMV-14 (Sigma-Aldrich, St. Louis, MO, USA). KYN-2 cells were transfected with LGR5-FL or empty vector using Lipofectamine LTX reagent (Invitrogen, Carlsbad, CA, USA). Production of LGR5-FL protein was detected by confocal laser scanning microscopy (LSM510, Carl Zeiss, Germany) and western blot analysis, using the FLAG M2 antibody (Sigma-Aldrich). F-actin was stained with TexasRed X-phalloidin (Molecular Probes, Eugene, OR, USA) and nucleus was stained with VECTASHIELD Mounting Medium with DAPI (Vector Laboratories Inc. Burlingame, CA, USA). Anti-E-cadherin (ALX-804-201-C100, Enzo Life Sciences, Inc.) and anti-β-catenin (E-5, Santa Cruz Biotechnology, Inc.) antibodies were used for immunofluorescent staining. Colonies that formed in 0.3% soft agar medium containing G418 (Invitrogen) were picked and propagated. Each colony was purified by three sequential series of limiting dilutions. Ultimately, six LGR5-transfected clones (KY-B1, KY-G1, KY-G2, KY-G6, KY-F3, and KY-S1) and five empty vector-transfected clones (KY-V2, KY-V3, KY-V4, KY-V5, and KY-V6) were established. Protein levels were analyzed by western blotting and mRNA levels were analyzed by quantitative PCR. Canonical Wnt signaling activity was measured with the TCF-luciferase reporter system (TOPflash/FOPflash, Upstate Millipore Co.), and the results are shown as the ratio of TOPflash to FOPflash (TOP/FOP).

Quantitative polymerase chain reaction (qPCR)

Total RNA was isolated from cells using the RNeasy Mini Kit, including DNase treatment (Qiagen KK, Tokyo, Japan). cDNA was synthesized using the PrimeScript® RT reagent kit (Perfect Real Time; Takara Bio, Shiga, Japan), and qPCR was performed on a Thermal Cycler Dice Real Time System using SYBR *Premix Ex Taq*™ (Perfect Real Time; Takara Bio). The primer sequences for qPCR were as follows: GAPDH forward, 5′–ATCATCCCTGCCTCTACTGG-3′; GAPDH reverse, 5′–TTTCTAGACGGCAGGTCAGGT-3′; LGR5 forward, 5′–GAGGATCTGGTGAGCCTGAGAA-3′; LGR5 reverse, 5′–CATAAGTGATGCTGGAGCTGGTAA-3′; RSPO1 forward, 5′–AAGGCTGTGAGCTCTGCTCT-3′; RSPO1 reverse, 5′–ATGTCGTTCCTCTCCAGCAG3′. GAPDH was used as a reference. Fold induction values were calculated using the $2^{-\Delta\Delta\ Ct}$ method. All experiments were performed in triplicate and repeated at least three times in separate experiments; representative data are shown.

Cell proliferation, cell migration, and cytotoxicity assays

Cells were plated in 24-well dishes, and the number of cells was counted in a hemocytometer after staining with trypan blue. Ratio number of cells represents the total mean number of LGR5-overexpressing cells or empty vector cells for each day compared to the total mean number of cells at day 0. RNA interference experiments were performed using siRNA. The target sequences were as follows: LGR5-585, 5′–GAA CAA AAU ACA CCA CAUA-3′; LGR5-662, 5′–GAA UCC ACU CCC UGG GAAA-3′. AllStars Negative Control siRNA (Qiagen) was used as a control. Cells were transfected with the final concentration of 10 nM siRNA using Lipofectamine RNAiMAX transfection reagent (Invitrogen).

For cytotoxicity tests, cells were treated with puromycin for 20 h, washed with PBS and covered with growth medium containing 0.3% agar. Cells were cultured for 2 weeks with occasional replenishment of the medium. Colonies were stained

with nitro blue tetrazolium reagent and photographed for counting. For cell migration assays, cells were placed in six-well dishes and incubated for two days. The confluent monolayer cultures were scratched and photographed after 24 h. The width of each scratch was measured at ten points and more than five scratches were measured for each group. For RNA interference assays, cells were transfected with siRNAs for 20 h and replated in six-well dishes. The monolayer cultures that formed 24 h later were scratched and photographed as described previously.

Tumor formation assays

Clones containing LGR5-FL or empty vector were transplanted into the subcapsular region of the livers of NOG mice (NOD/Shi-scid/IL-2γ−/−) at 5×10^6 cells per mouse. The tumors that formed in the liver were resected, fixed with 10% neutral-formalin, and used for histological analysis. For metastasis assays, cells were inoculated into the subcapsular region of the spleens of NOG mice, and tumors that formed in the liver were used for histological analysis.

Statistical analysis

Differences were assessed for statistical significance using Student's *t*-test, with the level of significance being $P<0.05$.

Results

Establishment of LGR5-overexpressing clones

To determine the function of LGR5 in cancer cells, stable clones containing the LGR5 gene were established. We have tested several commercially available anti-LGR5 antibodies, however, we could not obtain good results in order to detect LGR5 protein expression in HCC tissue. Thus, we constructed a FLAG-tagged LGR5-expression vector (LGR5-FL), and production of the protein was detected by immunofluorescence microscopy and western blot analysis using anti-FLAG antibody. When LGR5-FL was transfected into KYN-2 cells, the protein was localized mostly in the cytoplasm and cytoplasmic membrane (Fig. 1A). To establish stable clones, LGR5-FL or empty vector was transfected into KYN-2 cells, and G418-resistant colonies that formed in soft agar medium were purified by three series of limiting-dilution propagations. Six clones stably transfected with LGR5-FL (KY-B1, KY-G1, KY-G2, KY-G6, KY-F3, KY-S1) and five clones stably transfected with empty vector (KY-V2, KY-V3, KY-V4, KY-V5, KY-V6) were isolated. The LGR5 protein (~100 kD) was detected by western bot analysis (Fig. 1B), and mRNA levels were measured by qPCR (Fig. 1C). The KY-G1 and KY-S1 transfectants expressed high levels of LGR5 protein and mRNA. The protein and mRNA levels in each of the clones were well correlated, and the same levels were maintained after several passages. Only the results for three vector-transfectants are shown in Fig. 1B and C, but the other clones showed similar results.

Phase contrast microscopy showed that LGR5-overexpressing KY-G1 and KY-S1 cells had a round shape and aggregated together, whereas KY-V2 and KY-V3 cells had a flat extended shape and spread on the culture dishes (Fig. 1D). LGR5-transfectants stacked up on the surface of the culture dishes, whereas empty vector–transfectants formed flat monolayers (Fig. 1E). Phalloidin staining showed strong F-actin signals between KY-G1 cells (so-called cortical actin), whereas KY-V2 cells showed a flat extended shape with F-actin in the cytoplasm (Fig. 1F). Distinct fluorescent signals of E-cadherin were located between KY-G1 cells (Fig. 1G). Similar distribution of β-catenin was also seen in KY-G1 and KY-V2 cells, respectively (Fig. 1H). Accumulation of β-catenin in nuclei which is often seen in cell with activated Wnt signaling could not be detected in LGR-5 overexpressing KY-G1 cells. Non-adherent cultures of KY-G1 cells formed spherical shapes and most of the cells in the center survived intact, whereas KY-V2 cells formed irregular spheres and some of these had a necrotic area at the center (Fig. 1G).

Overexpression of LGR5 promotes HCC cell viability, enhances colony formation, and decreases cell motility

The rates of proliferation of KY-G1 and KY-V2 cells were identical until cell numbers reached a maximum, however, KY-G1 cells survived longer in overgrowth conditions (Fig. 2A). Substantial numbers of KY-G1 cells survived after two weeks in overgrowth culture, whereas KY-V2 cells detached from the surface of the dishes and only a small proportion of cells survived in overgrowth culture (Fig. 2B). In addition, KY-G1 cells were more resistant to the toxicity of puromycin (Fig. 2C), and also formed soft agar colonies more efficiently than KY-V2 cells (Fig. 2D). The motility of the cells was measured by performing scratch tests on confluent cell cultures. Retardation of cell migration was observed as early as 5 h in KY-G1 cells (data not shown), and scratch scars were repaired more rapidly at 24 h in KY-V2 cell cultures than in KY-G1 cell cultures (Fig. 2E). The reduction ability of LGR5-overexpressing cells to migrate after scratch wound assay was also previously reported in colorectal carcinoma cell lines [10].

LGR5-overexpressing HCC cells forms nodular tumors with decreased infiltration and metastatic foci

To further evaluate the function of LGR5 in vivo, KY-G1 or KY-V2 cells were transplanted into the subcapsular region of the livers of NOG mice. KY-G1 cells formed tumors with trabecular pattern in the liver, while KY-V2 cells formed tumors with ill trabecular pattern (Fig. 3A a, b). Expression of LGR5-FL was detected in the tumors formed by KY-G1 cells but not in the tumors formed by KY-V2 cells (Fig. 3A a, b inserts). Reticulum staining showed a trabecular pattern in the KY-G1 tumors, whereas a solid pattern was observed in the KY-V2 tumors (Fig. 3A c, d). Infiltration into the vicinal muscle tissues was rare in the tumors formed by KY-G1 cells, but occasionally seen in the tumors formed by KY-V2 cells (Fig. 3A e, f). When KY-G1 cells were transplanted into the subcapsular region of the spleen, the number of metastatic foci in the liver, and the number of micrometastases into the portal veins was lower, compared with transplantation of KY-V2 cells (Fig. 3B a–c). In addition, tumors formed by KY-V2 cells showed a wider area of hemorrhagic necrosis compared with those formed by KY-G1 cells.

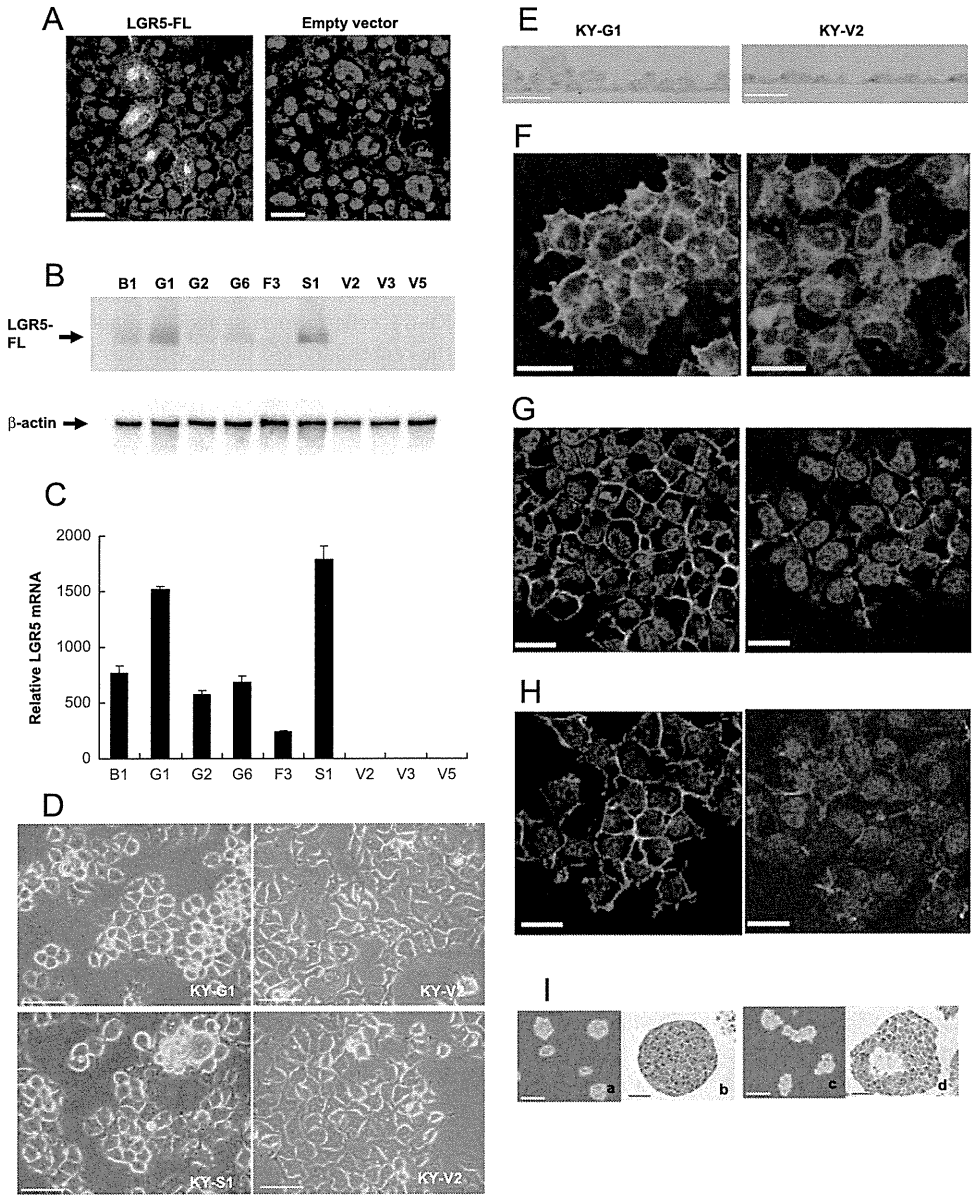

Fig. 1 – Establishment of LGR5-overexpressing clones. A: Immunofluorescent staining of KYN-2 cells transiently transfected with LGR5-FL or empty vector. Cells were stained with anti-FLAG antibody. Green: LGR5. Red: F-actin. Blue: nuclei. Bar, 50 μm. B: Western blot analysis of LGR5-overexpressing clones (KY-B1, KY-G1, KY-G2, KY-G6, KY-F3, KY-S1). KY-V2, KY-V3 and KY-V5 were stable transfectants containing empty vector. Blots were stained with anti-FLAG antibody (upper) or anti-β-actin antibody (lower). C: Expression of LGR5 mRNA in stable transfectants. Relative LGR5 mRNA level was shown as fold increase when the average level of non-transfected KYN-2 was set at 1. D: Morphology of clones containing LGR5-FL (KY-G1 and KY-S1) or empty vector (KY-V2 and KY-V3). (Bar, 100 μm) E: Vertical sections of 3-day cultures. KY-G1 and KY-V2 cells were embedded in EPON resin and sliced sections were stained with toluidine blue. F: Distribution of F-actin. F-actin was visualized by staining with phalloidin. Bar, 100 μm. G: Localization of E-cadherin (Green: E-cadherin, Blue: nuclei, Bar, 50 μm). H: Localization of β-catenin (Green: E-cadherin, Blue: nuclei, Bar, 50 μm). I: Morphology of non-adherent cultures of KY-G1 (a, b) and KY-V2 (c, d). Photographs show phase contrast microscopy (a, c. Bar, 200 μm) and HE staining of paraffin embedded sections (b, d. Bar, 500 μm). E-I: KY-G1 (left column), KY-V2 (right column). (For interpretation of the references to color in this figure, the reader is referred to the web version of this article.)

Down-regulation of LGR5 in HCC cells transforms cells to a loosely associated morphology and increased cell motility

To determine whether the characteristics of the KY-G1 cells were indeed due to the expression of higher levels of LGR5, we examined the effect of down-regulating LGR5 using siRNA. HepG2 cells were transfected with two siRNA sequences (si585 and si662) and LGR5 mRNA levels were analyzed by qPCR. LGR5 mRNA levels were significantly decreased 24–96 h after transfection of siRNAs against LGR5 (Supplementary Fig. 1; only 48 h data is shown). si662 suppressed expression of LGR5 more efficiently than si585, and similar results were obtained with